J. Fluid Mech. (1996), vol. 329, pp. 341–371

Active control in the turbulent wall layer of a minimal flow unit

By HENRY A. CARLSON[1] AND JOHN L. LUMLEY[2]

[1]Hughes Missile Systems Company, PO Box 11337, Tucson, AZ 85734, USA

[2]Department of Mechanical and Aerospace Engineering, Upson Hall, Cornell University, Ithaca, NY 14853, USA

(Received 26 April 1995 and in revised form 8 August 1996)

Direct simulations of flow in a channel with complex, time-dependent wall geometries facilitate an investigation of smart skin control in a turbulent wall layer (with skin friction drag reduction as the goal). The test bed is a minimal flow unit, containing one pair of coherent structures in the near-wall region: a high- and a low-speed streak. The controlling device consists of an actuator, Gaussian in shape and approximately twelve wall units in height, that emerges from one of the channel walls. Raising the actuator underneath a low-speed streak effects an increase in drag, raising it underneath a high-speed streak effects a reduction – indicating a mechanism for control. In the high-speed region, fast-moving fluid is lifted by the actuator away from the wall, allowing the adjacent low-speed region to expand and thereby lowering the average wall shear stress. Conversely, raising an actuator underneath a low-speed streak allows the adjacent high-speed region to expand, which increases skin drag.

1. Introduction

With skin friction drag reduction as the objective, control in the near-wall region of a turbulent flow is a problem that has received sustained attention. Modest reductions in drag can translate into significant savings in air transport fuel costs. Drag reduction as high as 10% has been achieved with wall-mounted, streamwise ribs or riblets – this being an example of passive control. See Bacher & Smith (1985), Bruse *et al.* (1993), Chu & Karniadakis (1993), and Walsh (1980). Active methods have included injection of polymers by Lumley (1973) and Virk (1975) and mass transport through porous walls by Choi, Moin & Kim (1994), for example.

Flow separation at struts and other interfaces is another major contributor to fuel costs; methods of active control of separation is an area of interest also driven by economic considerations. Control aimed at reducing Reynolds stresses, too, has potential for industrial application: these stresses and heat flux are well-correlated and lowering the heat transfer between exhaust gases from the combustor and the turbine blades in an aircraft gas turbine would increase the allowable operating temperature and boost efficiency.

Here, the controlling device is an actuator: a wall that contorts in time to produce flow structures that interact with and alter the naturally occurring dynamics in the near-wall region. From Kline *et al.* (1967), the morphology of wall-bounded, turbulent flow includes regions of high- and low-speed fluid (streaks), located near the wall, alternating in the spanwise direction, and aligned with the flow. From

Smith & Metzler (1983), these regions drift slowly in the cross-flow direction and persist through more than one peak in the evolution of spatially averaged wall shear stress. Except at very high Reynolds numbers the streak spacing, normalized with the inner variables, is a constant value. Streak lengths of more than ten times the spanwise spacing have been observed experimentally by Blackwelder & Eckelmann (1979).

The consensus is that primary mechanisms for the production of turbulent kinetic energy are an ejection phase, involving the low-speed fluid, and a sweep phase, involving the high-speed fluid. Although detailed explanations of these phenomena vary, ejection may be characterized as the transport of low-speed fluid away from the wall and sweep the transport of high-speed fluid toward the wall; see Corino & Brodkey (1969). The ejection generates Reynolds stress which, in turn, produces unstable inflectional profiles. This secondary instability culminates in a burst of higher wavenumber turbulence.

An increase in the frequency of the bursts causes a general increase in wall shear stress level. The term 'burst' is sometimes used for the whole cycle – ejection, instability, and sweep. Otherwise, it refers to the secondary instability, following the ejection. An increase in skin friction occurs during the sweep phase – as momentum is driven toward the wall – causing an increase in the streamwise strain rate. Quasi-streamwise vortices produce the updraughts and downdraughts associated with ejections and sweeps; see Robinson (1991).

Active control methods seek to counter these dynamical events through a change in the boundary conditions – a wall that either moves itself or moves fluid through itself (smart skins). Suction/blowing has been used by Laurien & Kleiser (1989) to control transition in a wall-bounded flow. Some strategies under consideration for active control in a turbulent boundary layer propose to suppress the ejection of low-speed fluid either by removing fluid through the wall or by raising an obstacle that will generate, presumably, one dominant pair of vortices with a central downdraught. Coller, Holmes & Lumley (1994) suggest that the crosswind produced by such a pair may be used to weaken an adjacent ejection pair. The reasoning in either of these schemes is that suppressing an ejection will mitigate the concomitant sweep (the two events being parts of an overall cycle). Taking a different tack, the idea here is to position an actuator underneath a high-speed streak in order to lift the fast-moving fluid away from the wall, without attempting to pre-empt or curtail lifting of the low-speed streak.

The numerical method, described in §2, consists of a spectral representation of the solution. Periodic boundary conditions in the streamwise direction yield the equivalent of an infinite array of actuators along the lower wall, aligned with the flow (one per minimal flow unit). Section 3 contains a description of the flow unit, chosen because it minimizes computational expense. Although the minimal unit is only a caricature of true, fully developed channel flow, it mimics features that are critical within the context of the control strategy: adjacent regions of high- and low-speed fluid. It also provides a manageable view of a complicated set of dynamics. Section 4 contains the results of an active control strategy.

2. The numerical method

The domain consists of a channel with a flat top wall and a bottom wall that may be perturbed in time from its initial, flat configuration. In Euclidian space, the streamwise, wall-normal, and spanwise directions are denoted as x_1, x_2, and x_3, respectively. Length, velocity, and time are non-dimensionalized, using the parameters

L_0, U_0, and L_0/U_0, respectively. U_0 is the mean streamwise velocity at mid-channel and L_0 is the channel half-height.

The top wall is located at $x_2 = +1$, the bottom wall at $x_2 = h-1$; $h(x_1, x_3, t)$ denotes the non-dimensionalized perturbation of the wall as the actuator rises. Through a time-dependent, three-dimensional curvilinear coordinate transformation (Voke & Collins 1984; Gal-Chen & Somerville 1975) the general domain is mapped to one that permits spectral representation of the solution (Canuto et al. 1988; Gottlieb, Hussaini, & Orszag 1984) and preserves exact boundary conditions.

Beginning with the Navier–Stokes equation in general tensor form, application of a metric operator effects the transformation. The primitive variables, velocity ($\boldsymbol{u}$) and modified pressure (p), may then be represented pseudospectrally: Fourier in the stream- and spanwise directions, Chebyshev wall-normal. In rotational form, the equation to be solved is

$$\frac{\partial u_i}{\partial t} = -\frac{\partial p}{\partial x_i} + \epsilon_{ijk} u_j \omega_k + \frac{1}{Re}\frac{\partial^2 u_i}{\partial x_j \partial x_j}, \tag{2.1a}$$

where

$$p \equiv \tilde{p} + \tfrac{1}{2} u_i u_i \quad \text{and} \quad \omega_i \equiv \epsilon_{ijk}\frac{\partial u_k}{\partial x_j}. \tag{2.1b}$$

The alternating tensor ϵ_{ijk} is $+1$ when i,j,k are in cyclic order, -1 when i,j,k are in anti-cyclic order, and 0 if any two of the i,j,k are equal. $\tilde{p}$ denotes the true pressure.

The Reynolds number (Re) is based on mean streamwise velocity at mid-channel (U_0) and on the channel half-height (L_0):

$$Re = \frac{U_0 L_0}{\nu}. \tag{2.2}$$

Viscosity is constant and the flow is solenoidal (incompressible):

$$\frac{\partial u_i}{\partial x_i} = 0. \tag{2.3}$$

Modified pressure is defined as a scalar function that, when substituted into (2.1a), satisfies (2.3) everywhere in the domain:

$$\frac{\partial^2 p}{\partial x_i \partial x_i} = \epsilon_{ijk}\frac{\partial}{\partial x_i}\left(u_j \omega_k\right). \tag{2.4}$$

Flow is sustained (viscous effects overcome) through the inclusion of a mean streamwise pressure gradient that maintains a constant mass flux:

$$\int_{h-1}^{1} \left\langle \frac{\partial u_1}{\partial t} \right\rangle_{k_{1,3}=0} \mathrm{d}x_2 = 0. \tag{2.5}$$

$\langle\cdot\rangle$ denotes Fourier decomposition and $k_{1,3} = 0$ corresponds to the mean value in a plane parallel to the walls. In the case of parabolic flow between two flat walls the gradient is $\langle \partial p/\partial x_1 \rangle_{k_{1,3}=0} = -2/Re$.

In general, displacement of the lower wall constitutes a change in the control volume. And with periodic conditions in the stream- and spanwise directions (no net mass flux), a solenoidal condition becomes irreconcilable. The problem is circumvented by specifying that the average wall perturbation is zero. This requirement is met by lowering the wall that surrounds the actuator.

Because the actuator volume is a small fraction of the total, the final perturbation of the surrounding wall (from its original position) is two orders of magnitude less than the final height of the actuator (0.001 versus 0.120). For this same reason the downward velocity of the surrounding wall is two orders of magnitude less than the upward velocity of the actuator itself. Exact boundary conditions for velocity are

$$u_1|_{x_2=\pm 1} = 0, \tag{2.6a}$$

$$u_2|_{x_2=+1} = 0, \tag{2.6b}$$

$$u_2|_{x_2=-1} = \frac{\partial h}{\partial t}, \tag{2.6c}$$

$$u_3|_{x_2=\pm 1} = 0. \tag{2.6d}$$

With an average wall perturbation of zero, the average cross-sectional area of the channel (normal to the flow) remains constant as an actuator grows or shrinks. This, in conjunction with the condition of constant mass flux as prescribed by (2.5), ensures that blockage will not be a factor when comparing flow in a flat-walled channel with flow in a channel with an actuator.

Boundary conditions for pressure are determined indirectly from the solenoidal condition via an influence matrix technique, developed by Kleiser & Schumann (1980). Velocity in the evolution equation is advanced in time by means of a three-step Runge–Kutta method; see Spalart, Moser & Rogers (1991). In the limit as $Re \rightarrow \infty$, the solution error attributable to temporal discretization approaches $(\Delta t)^4$. At the chosen Reynolds number the error falls between $(\Delta t)^3$ and $(\Delta t)^4$. In a variable mode the time step size finds its maximum based on a numerical stability condition (the conventionally defined CFL number) and is of order 10^{-2}.

With respect to spatial discretization the solution of flow in a canonical channel (zero wall perturbation) is spectrally accurate: the error is incurred through the truncation of the Fourier series. There is also round-off error associated with the fast Fourier transformation (FFT) subroutines. This round-off error, a machine-dependent quantity, is approximately 10^{-13}. Because covariant differentiation generates variable coefficient terms in the equations for pressure and velocity, an iterative solution scheme is required in the case of a non-canonical channel (non-zero wall perturbation). As a cost saving measure the number of required iterations is curbed by specifying a convergence tolerance of 10^{-7}, a value that falls between $(\Delta t)^3$ and $(\Delta t)^4$.

3. The minimal flow unit

Notwithstanding the previously mentioned cost saving measure, moving from a canonical channel (two flat, stationary walls) to a channel with a three-dimensional, time-dependent wall increases computational expense by a factor of thirty. Requirements for the spatial and temporal resolution of flow in a channel with a non-trivial boundary (along with iteration expense) far outweigh requirements for the adequate resolution of a turbulent field in the same computational box with trivial boundaries.

The cost of simulating turbulent flow in the canonical channel is a function of the size of the computational domain and the Reynolds number and is great enough, in and of itself, to have motivated others to search for ways of reducing the expense (while still obtaining information that can contribute to the investigation of wall-bounded turbulence). Through a series of numerical experiments, Jimenez & Moin (1991) have attempted to quantify a minimal flow unit, defined as the smallest computational box in which a turbulent channel flow may be sustained.

Flow parameters	Time parameters	Box dimensions	No of grid pts
$Re = 2000$	$\Delta t \approx 0.03$	$L_1 = \pi$	$N_1 = 48$
	$T \approx 1800$	$L_2 = 2$	$N_2 = 65$
		$L_3 = \frac{1}{2}\pi$	$N_3 = 24$

TABLE 1. Parameter values for the simulation of turbulent flow in a channel with flat walls

Their basic requirement for the flow is that it remain non-laminar, stochastic, and three-dimensional.

They determine that the critical parameter is box width. The minimum value is approximately equal to the experimentally observed average streak spacing: one hundred wall units. A box of this width contains one low- and one high-speed streak and yields low-order statistics that indicate a stationary, turbulent field. Although less precisely determined, the minimum length appears to lie between 250 and 350 wall units. Despite the fact that the minimum dimensions are expressed in wall units, there is some dependence upon Reynolds number. In general, slightly smaller boxes may be used at higher Reynolds numbers. Of course, higher Reynolds number flows require finer resolutions, which increase the expense.

Table 1 contains the parameter values that have been used here to produce a turbulent field in a channel with flat walls. Turbulence is generated by superposing a random perturbation upon a parabolic profile at $T = 0$. After approximately 300 (outer) time units, large transients due to the initial excitation have diminished. The simulation is terminated at $T = 1750$. Integrated over the interval from $T = 300$ to $T = 1750$, the time-averaged value of the mean streamwise strain rate at the lower wall is $\Omega_w = 4.868 U_0/L_0$. Local friction velocity and length scales may be defined as follows:

$$u_* = (\Omega_w \nu)^{1/2} \quad \text{and} \quad \delta_* = \left(\frac{\nu}{\Omega_w}\right)^{1/2}. \tag{3.1}$$

Using the given time-averaged value of Ω_w, relations between outer variables (u_i, x_i, t) and inner or wall variables (u_i^+, x_i^+, t^+) are

$$u_i^+ = (\Omega_w \nu)^{-1/2} u_i = (0.2054)\, u_i, \tag{3.2a}$$

$$x_i^+ = \left(\frac{\Omega_w}{\nu}\right)^{1/2} x_i = (98.67)\, x_i, \tag{3.2b}$$

and

$$t^+ = \Omega_w t = (4.868)\, t. \tag{3.2c}$$

As was stated in §2, outer units of velocity, length, and time are expressed in terms of U_0, L_0, and L_0/U_0, respectively.

From the dimensions of table 1 and (3.2*b*), the length, height, and width of the computational box are approximately 300, 200, and 150 wall units, respectively. In their minimal flow unit analyses, Jimenez & Moin (1991) use Reynolds numbers of 2000, 3000, and 5000. At the value of $Re = 2000$, they select box widths that are equal to or less than 110 wall units, and in each of these simulations the flow is turbulent at one wall, laminar at the other. In fact, for all boxes whose widths are equal to or slightly less than a critical value, the flows are one-sided, even at the higher Reynolds numbers. Extrapolating the data from their $Re = 2000$ simulations would indicate

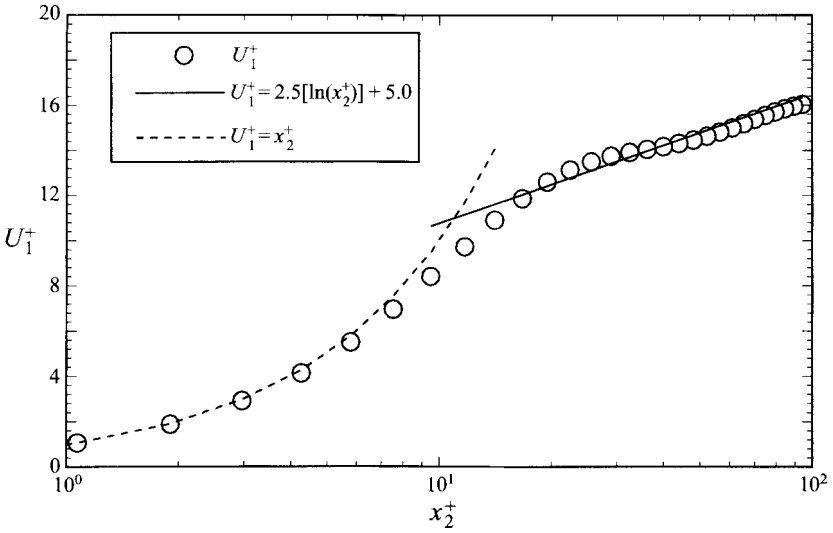

FIGURE 1. Time-averaged mean streamwise velocity profile in the lower half of the channel: U_1^+ as a function of x_2^+.

that a box width of 150 wall units lies just above the critical value corresponding to this Reynolds number.

Indeed, using the parameters of table 1, low-order statistics have been obtained that reflect, to a close degree, turbulent flow at both walls. The sample time for all of the statistics presented here is $\Delta t = 200$ ($\Delta t^+ \approx 1000$). Defining 'mean' as the spatially averaged value in a plane parallel to the walls, figure 1 is a profile of mean streamwise velocity in the lower half of the channel. The profile reveals a viscous sublayer that extends to $x_2^+ = 10$ and a logarithmic sublayer beginning at $x_2^+ = 20$. Statistical results for the upper channel half are omitted, as it is the bottom wall layer that will be the subject of investigation.

The velocity does slightly overshoot the log law at $x_2^+ = 25$; and a profile of mean streamwise velocity in outer units, covering the entire channel height, reveals small inflection points at $x_2 = \pm 0.4$, which are not consistent with fully developed channel flow. These anomalies stem from the small box width: the quasi-streamwise vortical structures, only two of which are characteristic of turbulent flow in the minimial flow unit, are approaching their minimal sustainable widths. These structures provide the mixing of momentum that determines the wall-normal distribution of mean streamwise velocity.

The Reynolds stress is defined as follows:

$$\tau_{ij} = -\langle u_i' u_j' \rangle_{k_{1,3}=0}. \tag{3.3}$$

The primes denote fluctuating values of velocity, and $k_{1,3} = 0$ corresponds to the mean value in a plane parallel to the walls. τ_{ij} has outer units of U_0^2. Figure 2 is a profile of τ_{12}^+ (the Reynolds stress normalized by u_*^2). A maximum/minimum of ± 0.66 at $x_2 = \mp 0.75$ is consistent with the two-sided turbulence results from Jimenez & Moin (1991) who, in turn, demonstrate that their minimal flow unit profiles compare favourably with experimental data for fully developed channel flow. The profile in figure 2 is not quite linear at mid-channel, and the location of zero Reynolds stress is slightly to the right of the channel centreline. These minor inconsistencies are attributable to the

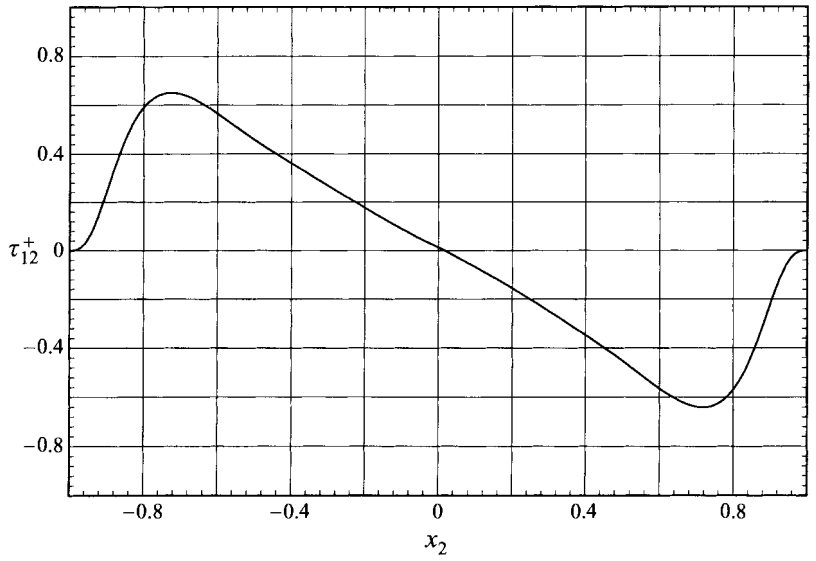

FIGURE 2. Time-averaged Reynolds stress profile in the lower half of the channel: τ_{12}^+ as a function of x_2.

finite sampling time and to the fact that only one pair of structures, rather than a multiplicity, is being sampled.

Figure 3 contains profiles of the RMS values of fluctuating velocity (defined as $|\tau_{ii}^+|^{1/2}$ with no sum on the indices). The values are normalized with the friction velocity (u_*). Peak values of the streamwise and wall-normal components and their locations ($x_2^+ = 15$ and $x_2^+ = 50$, respectively) match data from Jimenez & Moin (1991) who, again, demonstrate that their minimal flow unit profiles compare favourably with experimental data for fully developed channel flow.

Samplings of the kinetic energy spectra show acceptable drop-offs at the higher wave- numbers, which indicate that smaller scales in the turbulent field are adequately resolved. Plots of the velocity autocorrelation tensors as functions of stream- and spanwise separation reveal a distinctive feature of the minimal flow unit: the box size is too small for points at the largest separations to be uncorrelated, particularly in the case of streamwise velocity as a function of streamwise separation. As will be described in §4, the flow field consists of a periodic array of identical structures.

Jimenez & Moin (1991) identify another feature that is distinctive of the minimal flow unit: quantities such as wall shear stress and maximum vorticity are well correlated at each wall ($\geqslant 0.5$), whereas the correlations of quantities at one wall with those at the other are low ($\leqslant 0.15$), indicating that each wall layer evolves independently. In contrast, Blackwelder & Eckelmann (1979) report that the two wall layers do communicate with one another in fully developed channel flow.

4. An active control strategy

4.1. *The baseline simulation*

A time history of the mean streamwise strain rate at the lower wall, normalized by Ω_w, is shown in figure 4. The evolution of mean strain rate is quasi-periodic, consisting of several intermittency cycles. A cycle is defined here as the excursion from one minimum to the next. The inset of figure 4 magnifies one representative cycle,

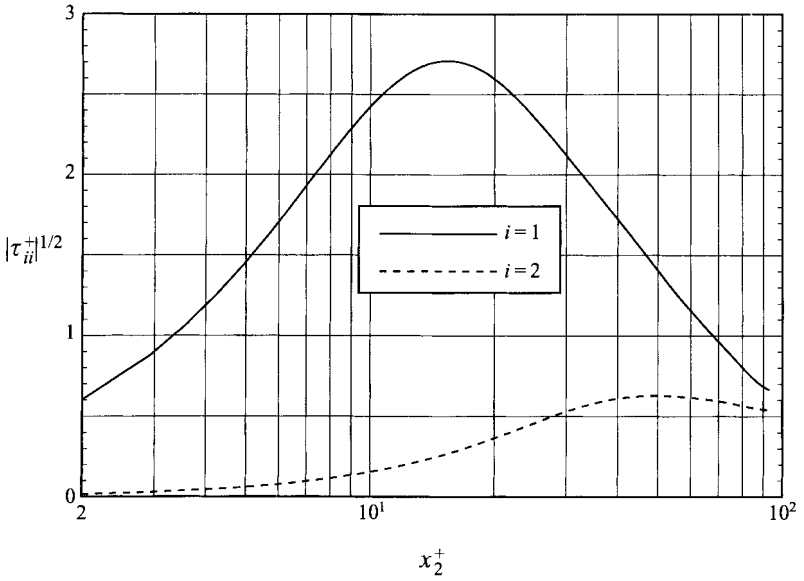

FIGURE 3. Time-averaged RMS fluctuating velocity profile in the lower half of the channel: $\left(|\tau_{ii}^+|\right)^{1/2}$ as a function of x_2^+.

chosen because the smooth evolution minimizes simulation time, thereby reducing the computational expense (which becomes significant with a perturbed wall).

Case 0 corresponds to flow over the unperturbed wall through one intermittency cycle, beginning at $T = 1349.3$ (figure 4 inset). Following a description of this baseline simulation, three control runs will be detailed (Cases 1, 2, and 3) in which actuators are raised at the onset of the cycle (at $T = 1349.3$). Finally, the effects of lowering an actuator will be examined in Cases 4 and 5.

Figure 5 is a time sequence for Case 0: contour plots of streamwise strain rate. Outer units are used in all contour plots. To convert lengths into wall units multiply by 100. Clearly depicted is a low-speed region centred at approximately $x_3 = 0.30$ and a high-speed region at $x_3 = 1.25$. As indicated in §3 (the discussion of the streamwise autocorrelation tensor as a function of streamwise separation), the structures extend from inlet to outlet. Their locations remain fixed throughout the cycle.

Samplings at longer time intervals indicate that lateral movement of the streaks is very gradual, approximately 0.1 wall unit (Δx_3^+) per unit of wall time (Δt^+). During the intermittency cycle the regions wax and wane: one expands and intensifies while the other shrinks. At $T = 1343.4$ as the mean strain rate approaches a minimum, the width of the high-speed region is approximately $\Delta x_3^+ = 30$. By the time the mean strain rate peaks at $T = 1363.3$, the width has doubled to $\Delta x_3^+ = 60$.

The behaviour of actual low-speed streaks in the near-wall region of a turbulent wall layer is more complicated than the dynamics that occur in a minimal flow unit, owing to the multiplicity of coherent structures. Smith & Metzler (1983) report an average streak lifespan of $\Delta t^+ \approx 480$ and observe streaks that persist for times as long as $\Delta t^+ = 2500$. During their lifespans, one streak may coalesce or merge with another, and streaks often divide. Nakagawa & Nezu (1981) suggest that, very near the wall, streaks continually combine and divide in essential equilibrium, during which time the average rate of lateral movement of an average structure is higher than the drift rate that is observed in the single structure of a minimal flow unit.

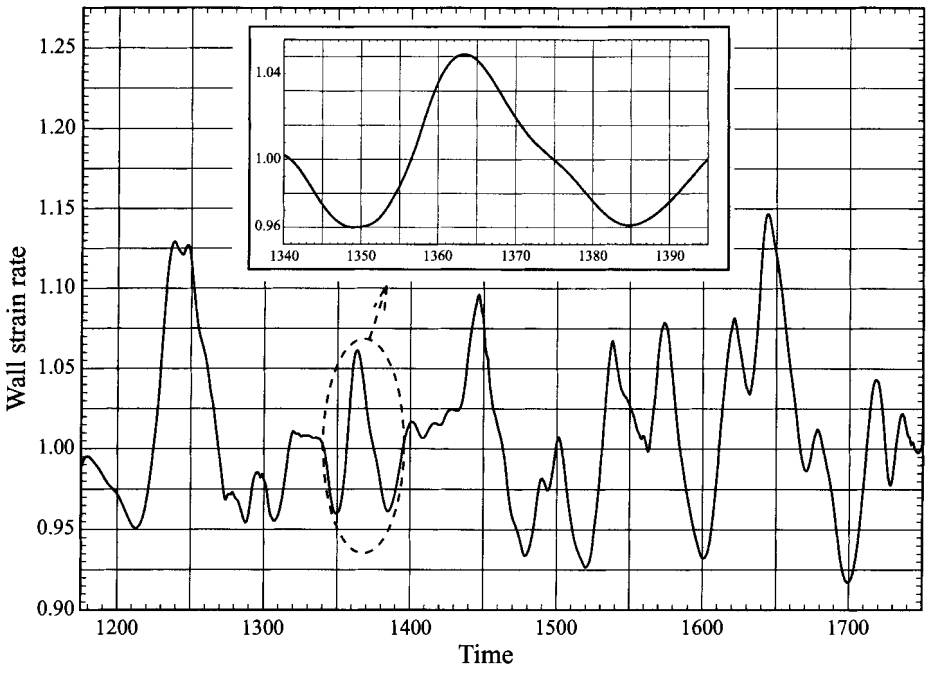

FIGURE 4. A time history for Case 0 of the mean streamwise strain rate at the lower wall, normalized with the time-averaged value (Ω_w). The inset delineates one representative intermittency cycle.

Figure 6 is a time sequence of contour plots of the spanwise strain rate, indicating the direction of cross-stream flow close to the wall. At either end of the cycle as the mean streamwise strain rate is on the wane ($T = 1343.4$ and $T = 1378.2$), no organized structures of the spanwise strain rate exist. During the rise in drag from $T = 1349.3$ to $T = 1363.3$, structures of opposite sense centred on the high-speed streak intensify, reflecting the expansion of the region.

Figure 7 is a time sequence of streamwise vorticity in a plane parallel to the wall at $x_2^+ = 16$. A pair of structures of opposite sense is born at $T = 1349.3$, centred directly above the high-speed streak and providing a downdraught of fluid into the region. The pair intensifies as drag increases and persists until approximately $T = 1363.3$. Figure 8 is a time sequence of surface stress patterns. Streamlines are constructed from the stream- and spanwise components of the strain rate, and they indicate flow direction close to the wall. The cross-flow perturbations or wiggles in the low-speed region may be understood within the context of an explanation, put forth by Jimenez & Moin (1991), of the ejection phase: the wrapping and lifting of a detached shear layer, a process closely akin to the classical hairpin model. Flow in the high-speed region is more ordered, clearly spreading apace with the increase in drag from $T = 1349.3$ to $T = 1357.9$.

4.2. *The set-up for control*

Turning now to control runs, the actuators of Cases 1, 2, and 3 are defined by the following Gaussian function:

$$h(x_1, x_3) = \varepsilon(t) \exp\left\{-\sigma^{-2}\left[(x_1 - x_1^0)^2 + \left(\frac{x_3 - x_3^0}{\mu}\right)^2\right]\right\}. \tag{4.1}$$

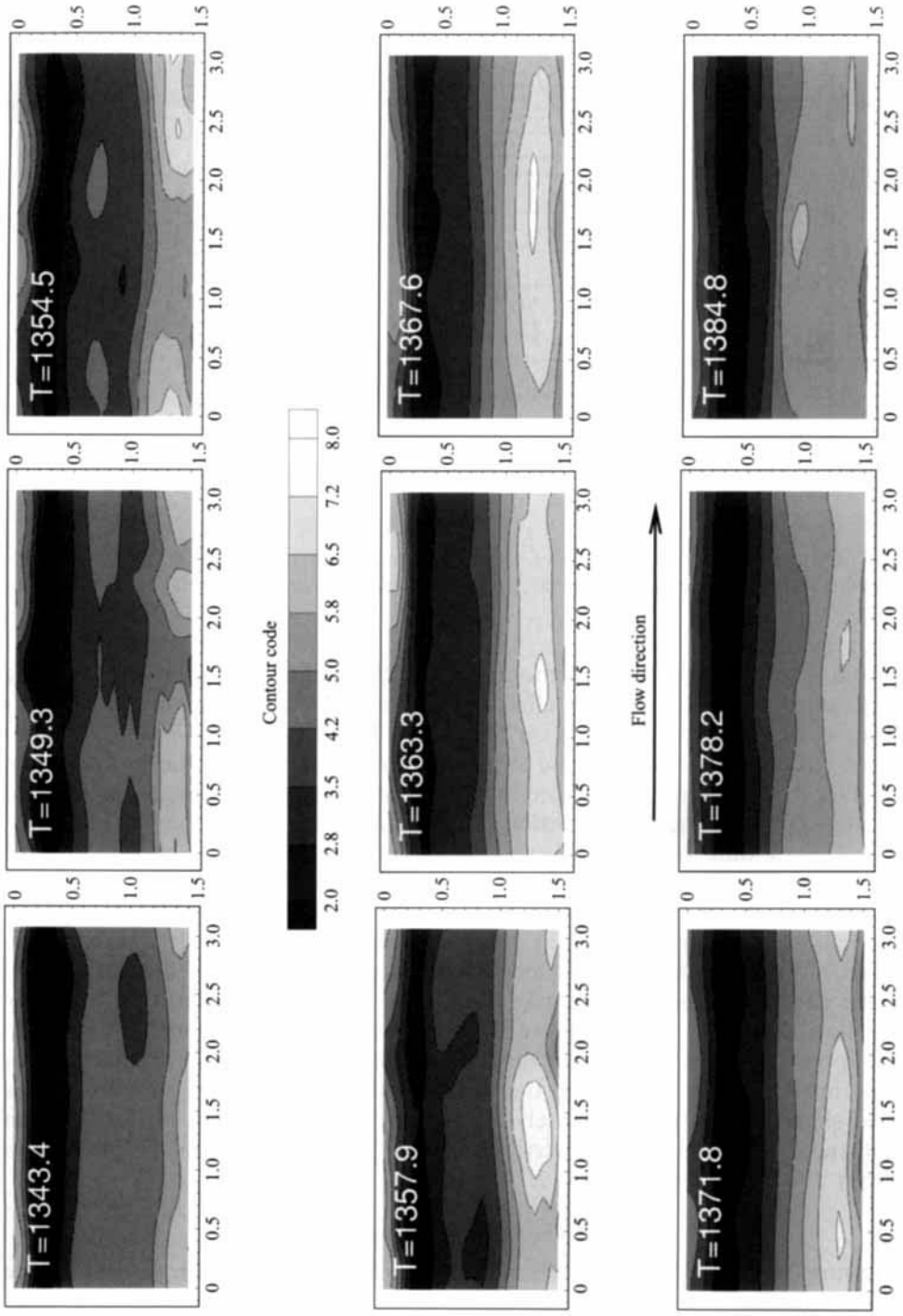

FIGURE 5. A time sequence for Case 0: contour plots of the streamwise component of strain rate at the lower wall (in outer units).

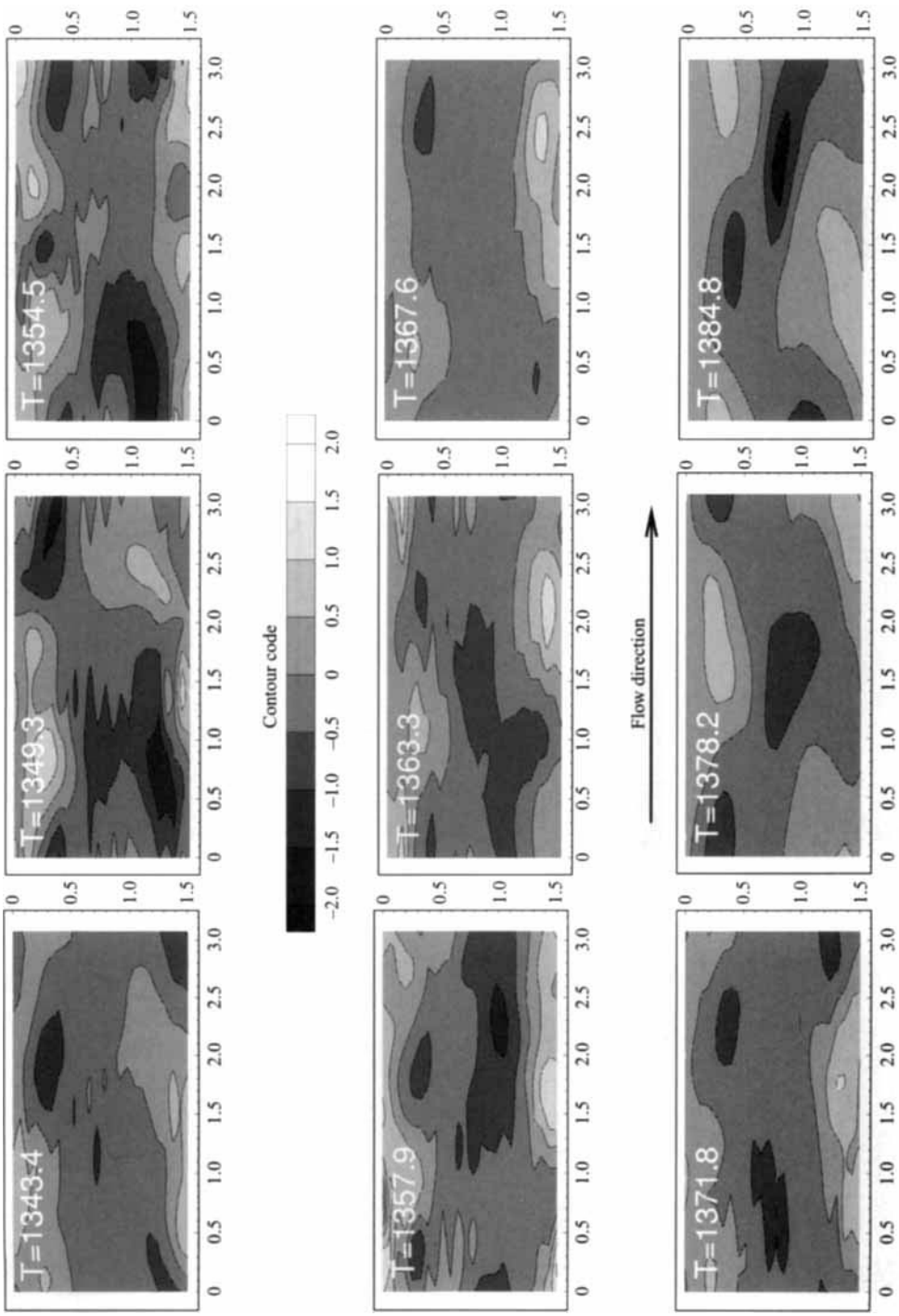

FIGURE 6. A time sequence for Case 0: contour plots of the spanwise component of strain rate at the lower wall (in outer units).

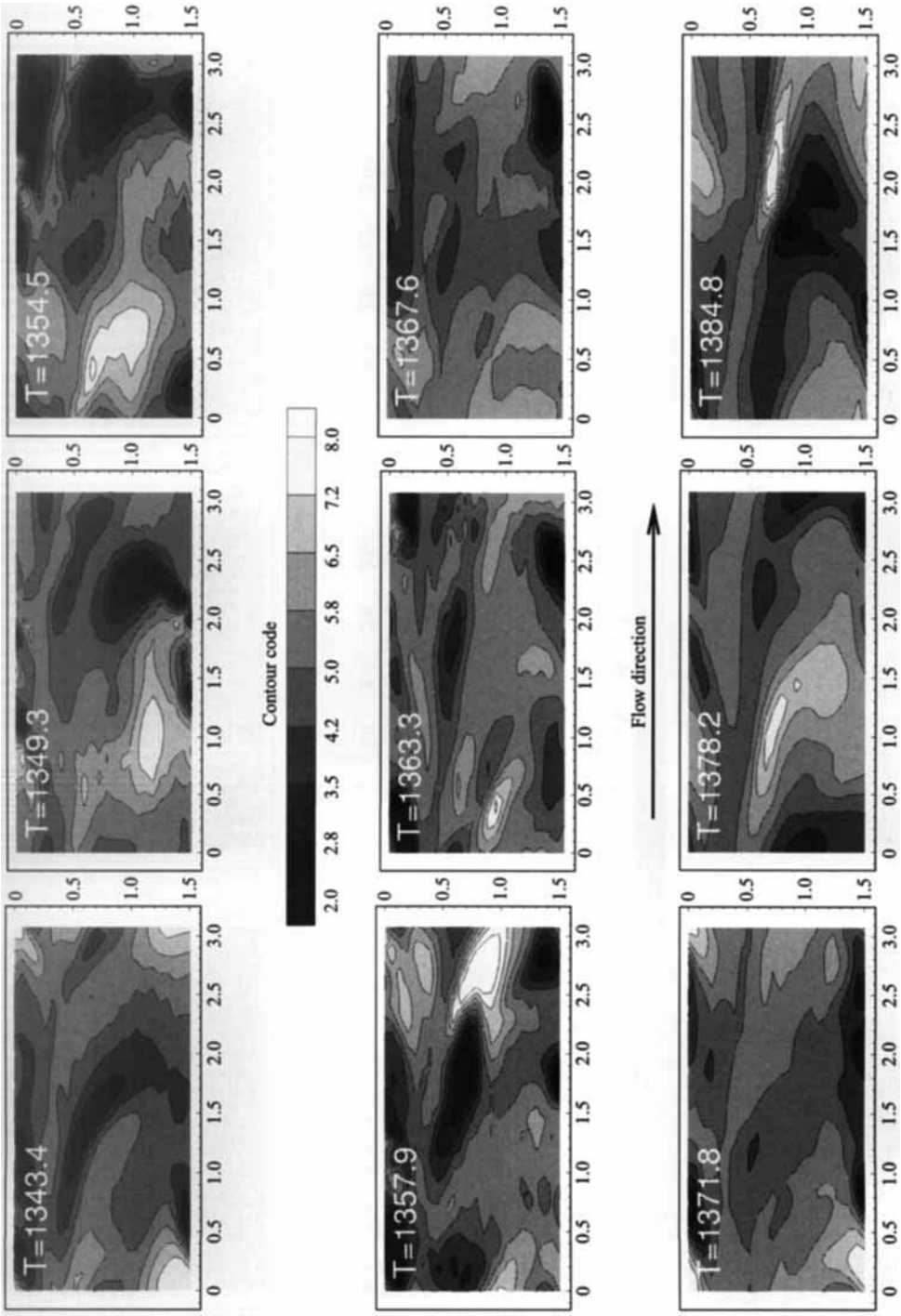

FIGURE 7. A time sequence for Case 0: contour plots of streamwise vorticity (in outer units). The view plane is located at $x_2 = -0.84$ ($x_2^+ = 16$).

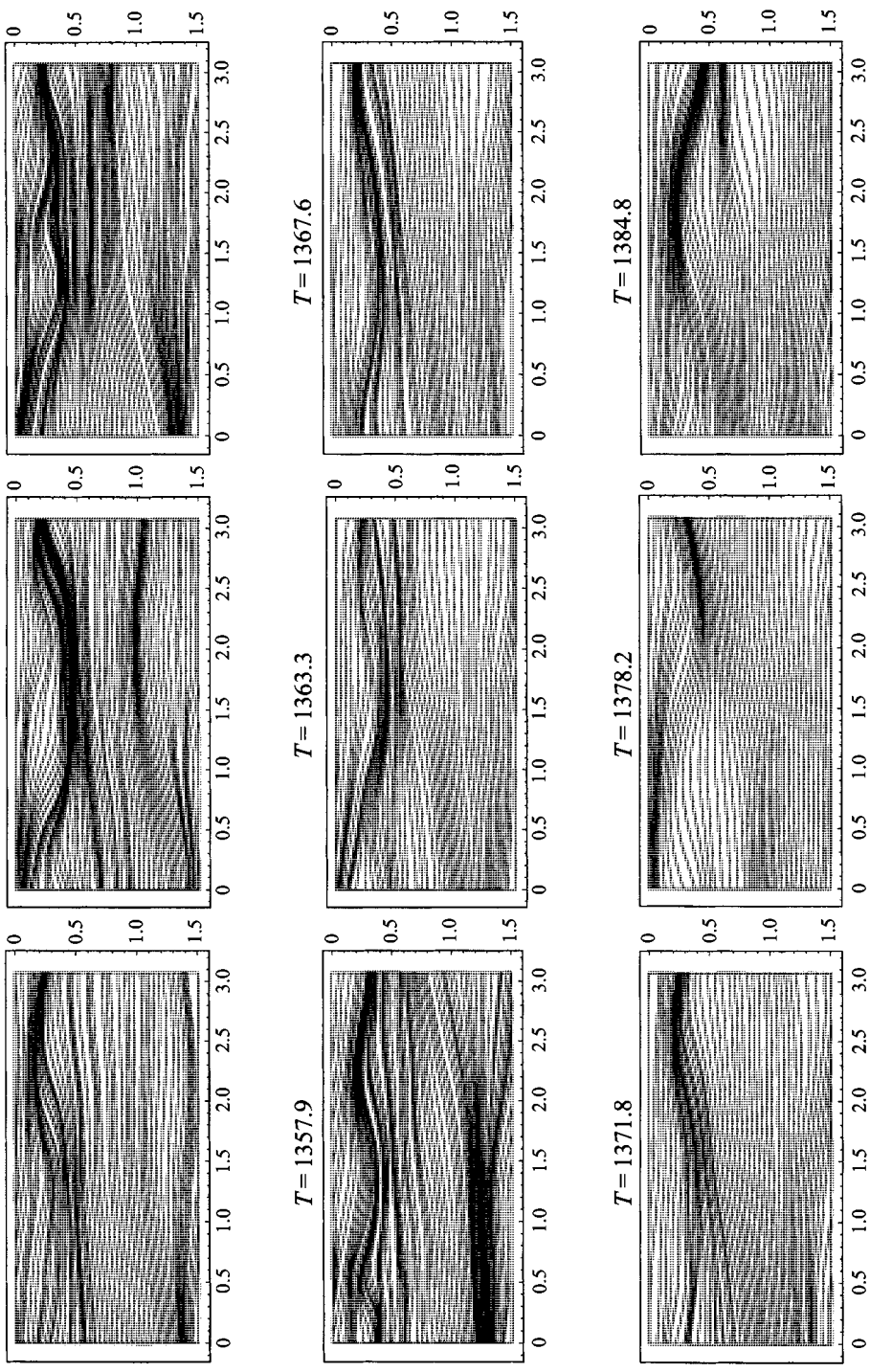

FIGURE 8. A time sequence for Case 0: surface stress patterns. Streamlines are constructed from the stream- and spanwise components of the strain rate and indicate the direction of flow close to the lower wall.

Flow parameters	Actuator parameters	Time	Box size	Resolution
$Re = 2000$	$\varepsilon_* = 0.12$	$\Delta t \approx 0.014$	$L_1 = \pi$	$N_1 = 80$
	$\sigma = 0.18$	$T \approx 30$	$L_2 = 2$	$N_2 = 65$
	$\dot{\varepsilon}_* = 0.05$		$L_3 = \frac{1}{2}\pi$	$N_3 = 32$
	$\ddot{\varepsilon}_c = 0.10$			
	$x_1^0 = \frac{1}{2}\pi$			

TABLE 2. Parameter values that are common in the first three control tests

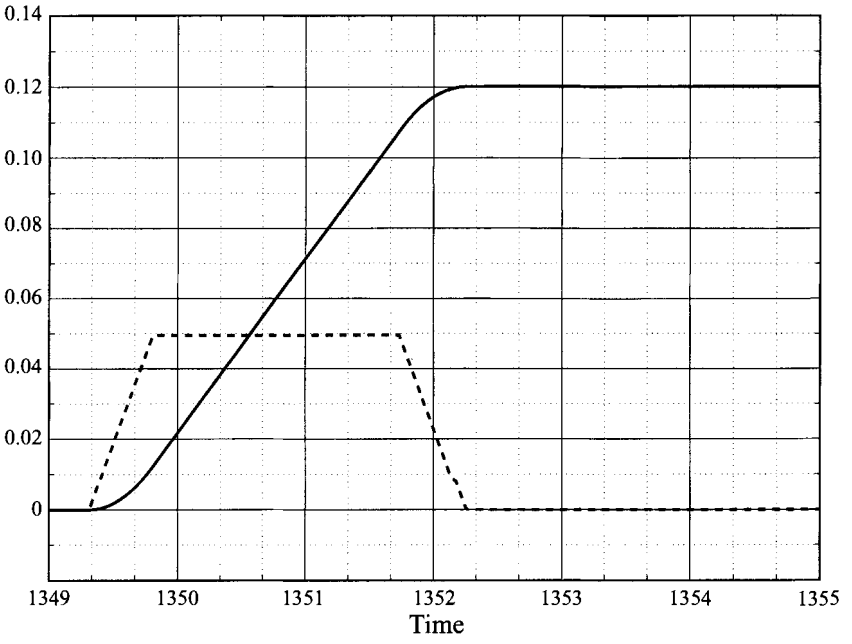

FIGURE 9. Actuator height (———) and velocity (- - - - -) as functions of time in outer units (Cases 1, 2, and 3).

Parameters whose values are common in the first three control tests are listed in table 2. Finer resolution requirements in the streamwise direction reduce the average time step size which, in conjunction with the iteration requirements (an average of five per sub-step), drives up the computational expense. Measured as hours of CPU time per unit of simulation time, the cost increases from approximately 0.0525 to between 1.5 and 2.0.

From (4.1) the height of an actuator (ε) is time-dependent, the standard deviation (σ) is not, so that the obstacle rises uniformly, as opposed to inflating like a balloon. Accelerating at a constant positive value ($+\ddot{\varepsilon}_c$) until a maximum velocity ($\dot{\varepsilon}_*$) is attained, each actuator continues to rise at this maximum speed. With the target height (ε_*) as input a controller determines when to decelerate the actuator (at $-\ddot{\varepsilon}_c$) so that it arrives at its target height with zero velocity (see figure 9). In wall units the final height is $\varepsilon_*^+ = 12$, so that the tops of the actuators lie just above the viscous sublayer. The maximum speed is equal to the friction velocity, $\dot{\varepsilon}_* = u_*$, resulting in a rising time that is approximately 10% of the total length of the intermittency cycle.

Parameter	Case 1	Case 2	Case 3
x_3^0	$\frac{2}{5}\pi$	$\frac{1}{10}\pi$	$\frac{2}{5}\pi$
μ	1.0	1.0	2.0

TABLE 3. Parameter values that distinguish the first three control cases.

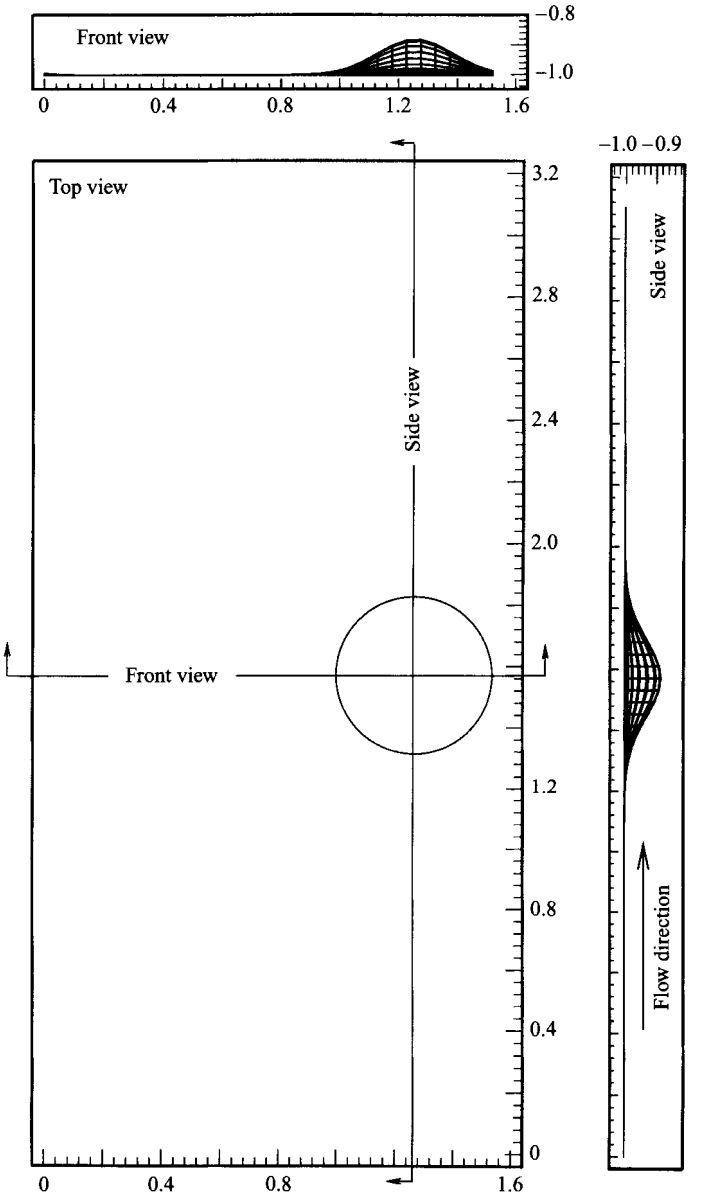

FIGURE 10. Views of the Case 1 actuator, indicating position and shape.

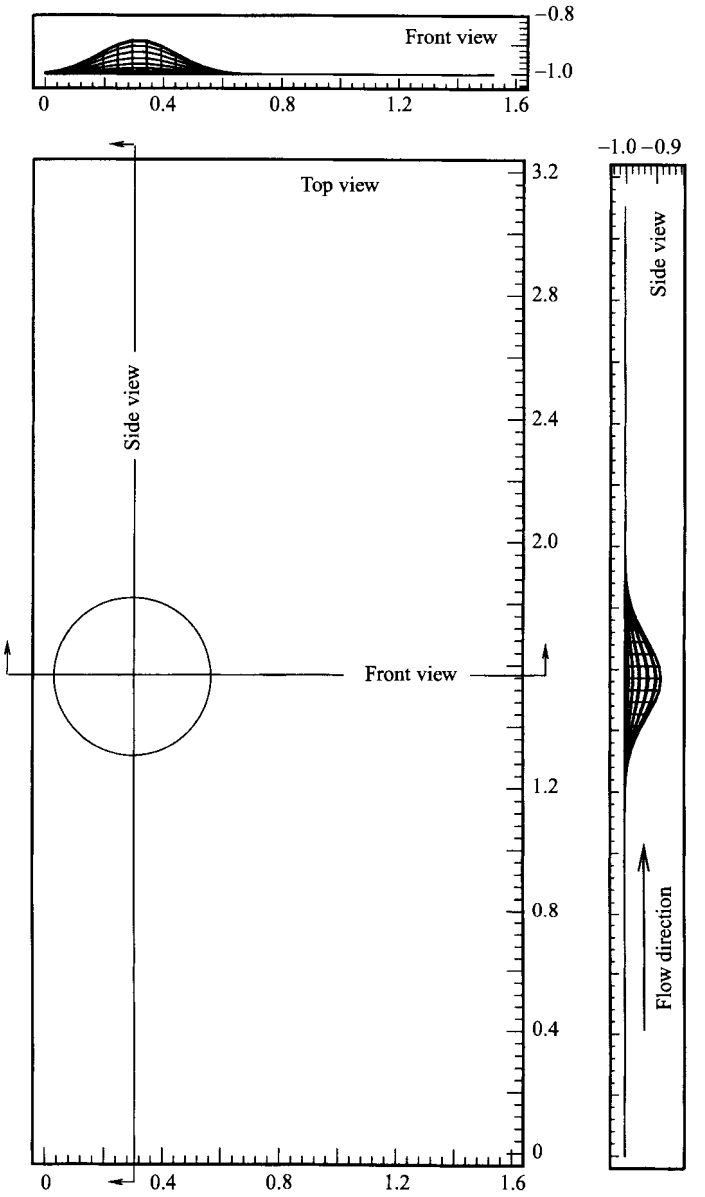

FIGURE 11. Views of the Case 2 actuator, indicating position and shape.

Parameter values that distinguish the first three control cases are listed in table 3. As has been shown, the most identifiable structures in the flow are the high- and low-speed streaks. In beginning an investigation of control this motivates one to consider using these structures as points of reference in determining where to raise an actuator. From a practical standpoint the attractiveness in such a scheme lies in the fact that cues from the flow to the actuator would consist of measurements of streamwise wall shear stress, taken *at the wall*, providing as strong a signal as exists in the flow, and representing the object of control itself. Preliminary fact-finding runs, Cases 1 and 2, are simulations of flow over actuators raised underneath the high- and

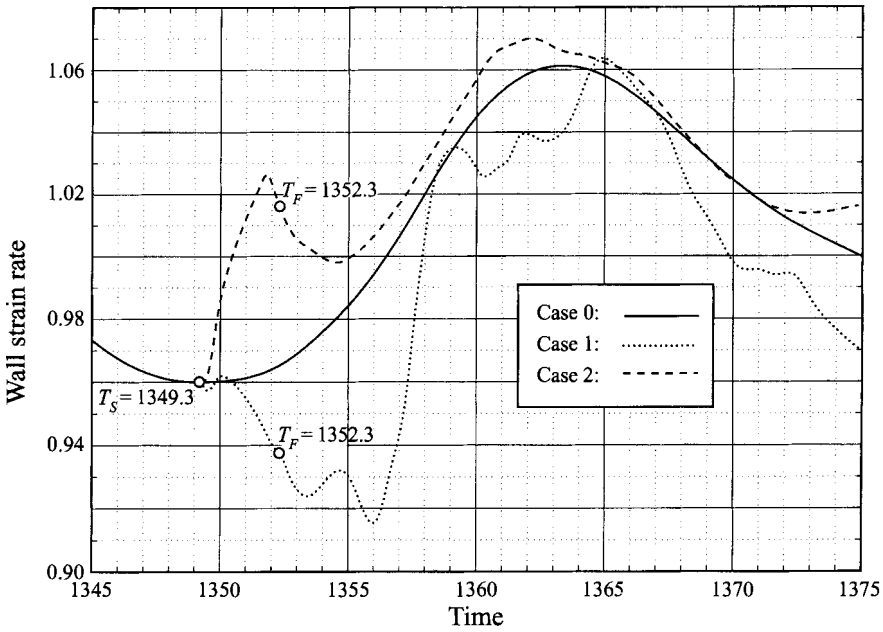

FIGURE 12. Time histories for Cases 0, 1, and 2 of the mean streamwise strain rate at the lower wall, normalized with the Case 0 time-averaged value (Ω_w). The actuators begin to rise at T_S and reach their target heights at T_F.

the low-speed streak, respectively. Figures 10 and 11 are views of the two actuators, indicating locations and shapes.

Time histories of the mean streamwise strain rate (Cases 0, 1, and 2) are provided in figure 12. The rising time of each actuator is approximately 3.0 in outer units. Drag trends downward in Case 1 during the first seven time units, then increases sharply for three. Presentation of a detailed picture of the dynamics, using time sequences, will be deferred until the description of Case 3. An explanation of why actuator placement makes a difference in the evolution of wall shear stress requires a brief summary of some relevant information.

4.3. *Background information: laminar flow over an actuator*

Simulations of laminar flow over an emerging obstacle have been performed using the same computational box, the same Reynolds number, and the same actuator parameters (height, shape, speed, acceleration); see Carlson & Lumley (1996). An initially parabolic profile, rather than a turbulent field, allows a clearer view of the dynamics associated with a rising actuator. Vortical structures are produced that are identical to those found in flow over a stationary obstacle (see Mason & Morton 1987), intensified and stretched by the upward velocity of the boundary. The flow structures consist of nested pairs of vortices up- and downstream of the actuator.

Closest to the wall are a pair with central upwash (upstream) and a pair with central downwash (downstream). Stacked atop these are weaker pairs of opposite sense. The pairs closest to the wall are produced by spanwise pressure gradients that act to divert flow around the obstacle upstream and back in behind it downstream. As the actuator rises, structures intensify by a factor of two and extend to three times their steady-state lengths, assuming more vertical attitudes as they are lifted by the actuator. Following deceleration to a stationary position this amplification

leads to a transient, triggering temporary re-attachment on the downstream side and a subsequent break in the vortical structures in the wake region as the flow evolves toward its steady state. The time scale of the transient is a direct function of the rising time of the actuator.

Contour plots of the streamwise strain rate at the wall reveal that a stagnation zone appears upstream as the actuator rises. Additionally, a region of high strain rate, located atop the actuator, grows and intensifies in time, reaching a maximum of $+12.0U_0/L_0$. As a baseline value, the streamwise strain rate at the wall, corresponding to a parabolic profile (absent the actuator), is $+2.0U_0/L_0$. Flow is separated in the wake region with a minimum strain rate of $-2.0U_0/L_0$. The upstream stagnation zone disappears after the actuator has decelerated to its final height.

4.4. *Control simulations (continued)*

Returning to figure 12 and the turbulent field, drag reductions are effected in Case 1 by the upwash pair of vortices, upstream of the actuator, which lifts high-speed fluid away from the wall, allowing the adjacent low-speed region to expand. To be shown in detail accompanying the discussion of Case 3, increases in drag occur when the downwash pair detaches downstream, travelling to the exit and back in at the entrance, positioning itself above the upstream pair and thereby cancelling the lifting process.

In Case 2 the initial increase in drag is effected by the upstream upwash pair as it pushes low-speed fluid away from the wall, allowing faster moving fluid from the adjacent high-speed region to expand. A temporary interruption in this occurs as detached downwash vortices, re-entering the box, reach the upstream side of the actuator. Because of these interruptions (in both Cases 1 and 2), net changes in drag are slight: approximately 2%. Form drag, one of the costs of control, is minimal in the case of either actuator: 0.3% of the time-averaged mean skin friction drag. Form drag is defined as follows:

$$F_1 = \int_S \tilde{p}\boldsymbol{n}\cdot\boldsymbol{e}_1 \mathrm{d}S. \tag{4.2}$$

S is the actuator surface, $\boldsymbol{n}$ is the vector normal to that surface, $\boldsymbol{e}_1$ is the unit vector in the streamwise direction, and $\tilde{p}$ is pressure.

Notwithstanding the low reduction in skin drag effected by the Case 1 actuator, identification of a mechanism for control holds promise and the next step is to optimize the effect through an adjustment of actuator parameters. Time sequences of the streamwise strain rate for Case 0 (figure 5) show that during the course of the intermittency cycle the width of the high-speed region doubles to $\Delta x_3^+ = 60$. The width of the Case 1 actuator is $\Delta x_3^+ = 36$. Reasoning that lifting more of the high-speed fluid away from the wall will improve drag reduction, Case 3 is a modification of Case 1, consisting of an actuator twice as wide, centred under the high-speed streak – see (4.1) and table 3.

Figure 13 contains views of the actuator, indicating location and shape. Time histories of the mean streamwise strain rate for Cases 0 and 3 are provided in figure 14. Again, drag trends downward during the first seven time units, followed by a sharp increase. The initial reduction, approximately 14%, is over three times the initial reduction effected in Case 1. In the interest of maintaining a reasonable limit on the amount of space consumed by figures, the time sequences that follow cover only the first half of the intermittancy cycle. Supplementary descriptions of the dynamics during the second half of the cycle will be provided in words.

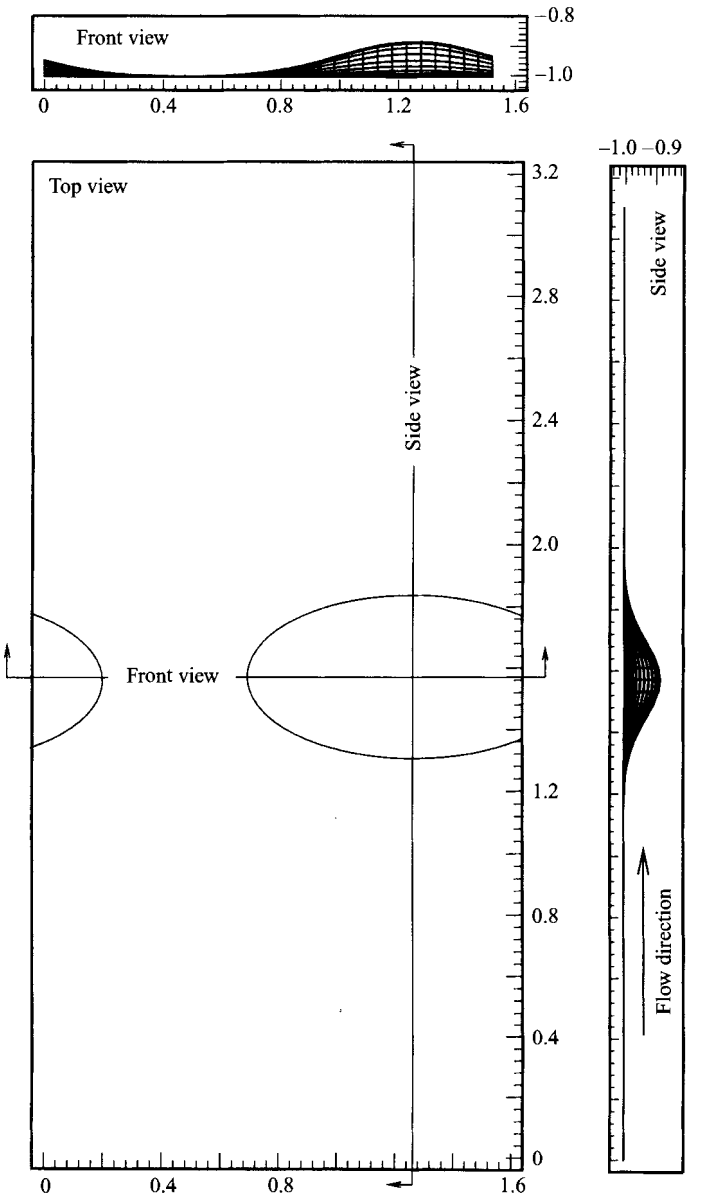

FIGURE 13. Views of the Case 3 actuator, indicating position and shape.

Figure 15 is a time sequence of contour plots of the streamwise strain rate for Case 3. As with the laminar flow (which was described in §4.1), an upstream stagnation zone appears and a zone of separated flow grows downstream as the actuator rises ($T = 1350.5$ and $T = 1351.6$). By the time the actuator stops at $T = 1352.7$, a region of high shear has appeared, signifying that fluid is accelerating rapidly over the top. This region intensifies in time. The maximum strain rate on top of the actuator reaches $+50.0U_0/L_0$ or approximately $+10\Omega_w$. Using a maximum value of $+25.0U_0/L_0$ in the plots, one-half the true maximum, captures better the lower-valued structures.

The downstream separation region modulates in time, due in part to the vortex shedding and in part to unsteadiness in the turbulent flow. The minimum value at

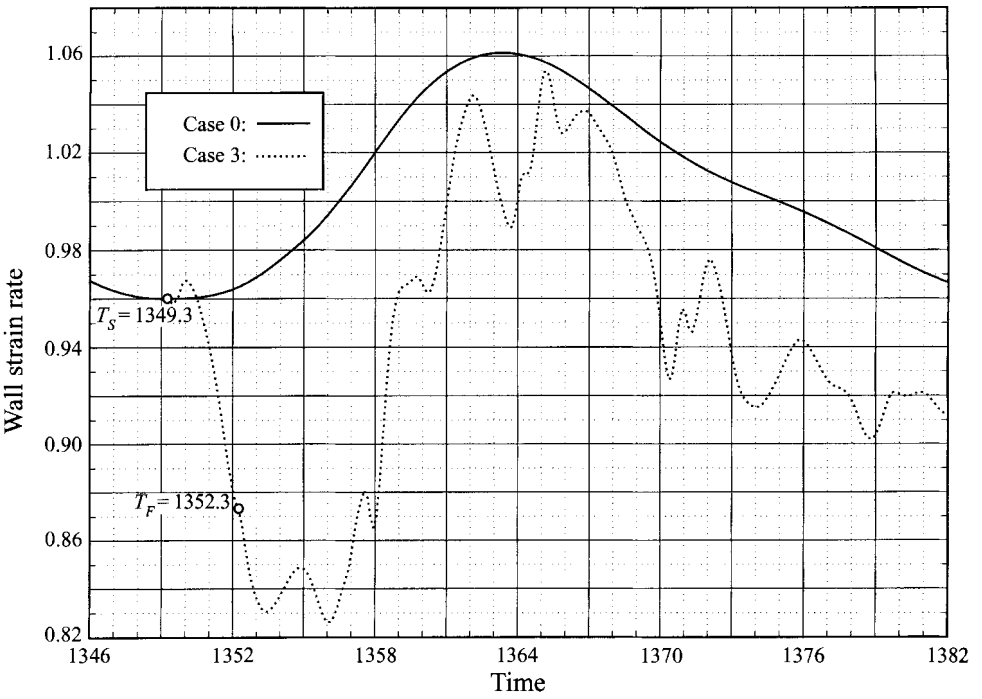

FIGURE 14. Time histories for Cases 0 and 3 of the mean streamwise strain rate at the lower wall, normalized with the Case 0 time-averaged value (Ω_w). The actuator begins to rise at T_S and reaches its target height at T_F.

the centre of the region is $-9.0U_0/L_0$ or approximately $-2\Omega_w$. The clearest sign of a disruption of the drag reduction process appears at $T = 1358.5$ (figure 15) when the high-shear region splits to form a patch of accelerating fluid to one side of the actuator. From figure 14 the mean drag has begun its most rapid ascent at this point in time.

Evidence of vortex shedding, which occurs once in the laminar case, is not as visible through the streamwise component of the strain rate as through the spanwise component: at the wall the spanwise strain rate is equivalent to streamwise vorticity (at least when the actuator is not moving). Figure 16 is a time sequence of the spanwise strain rate. As the actuator rises ($T = 1350.5$ and $T = 1351.5$) primary pairs of structures appear up- and downstream, reflecting divergence of flow on the approach and convergence behind. The upstream pair also signals an upwash overhead: lifting of high-speed fluid away from the wall. Maximum levels are approximately $1.25\Omega_w$.

At $T = 1352.7$ as the actuator stops, the primary upstream pair begins to elongate. By $T = 1353.7$ a break has occurred in the pair, signifying the onset of vortex shedding. The shed vortices in the wake counteract the lateral flow of low-speed fluid into the high-speed region and this coincides with a short-lived increase in drag (figure 14). At $T = 1354.8$ the secondary, downstream pair has re-entered the box and has combined with the primary pair upstream to form a broad area in which high-speed fluid is lifted from the wall. Again from figure 14, this coincides with the beginning of a short-lived decrease in drag.

At $T = 1355.6$ the primary upstream pair is contracting, prefacing an end to the drag reduction. At $T = 1357.1$, and to an even greater extent at $T = 1358.5$, broken structures re-entering the box have destroyed completely the cohesion of structures

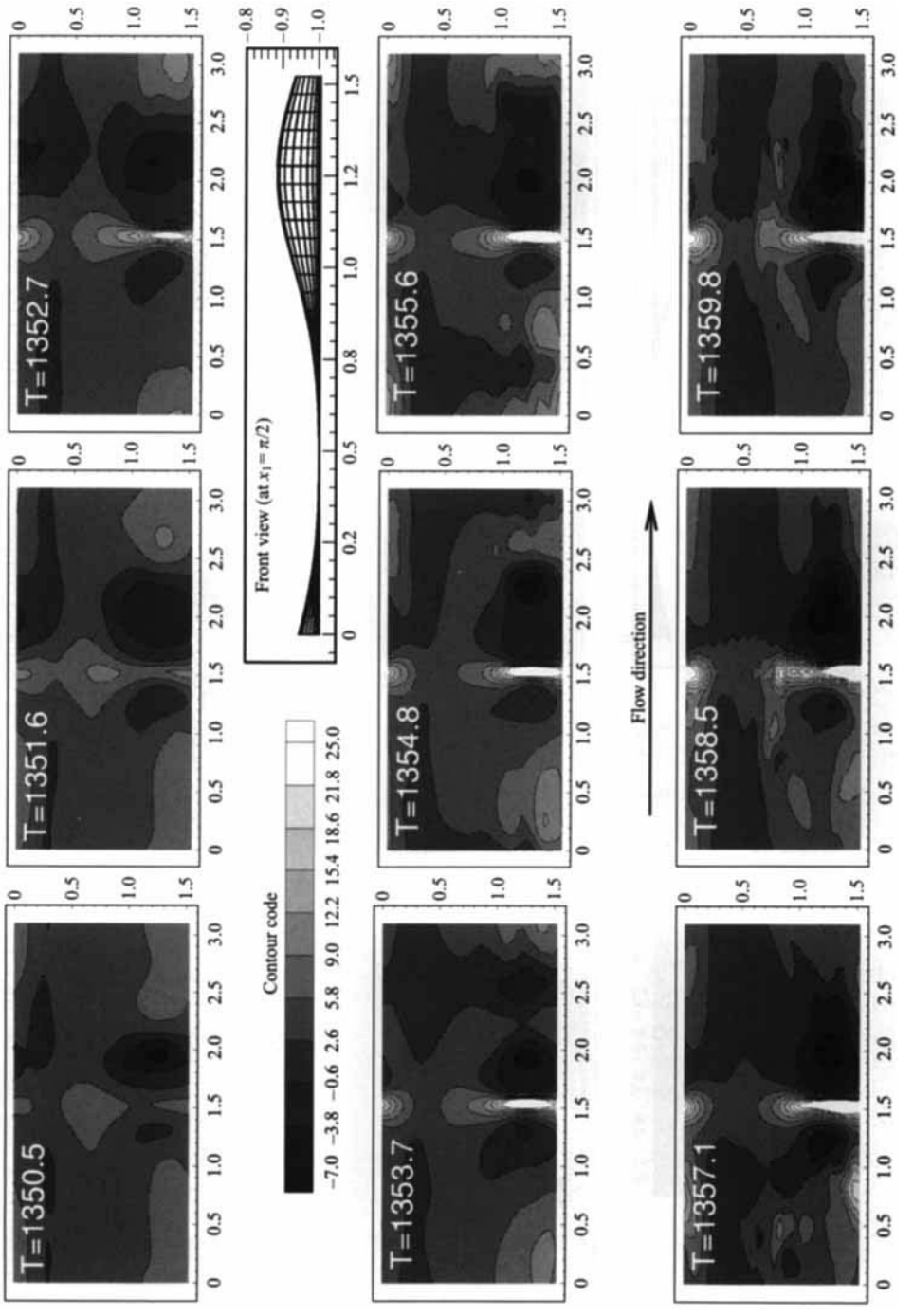

FIGURE 15. A time sequence for Case 3: contour plots of the streamwise component of strain rate at the lower wall (in outer units).

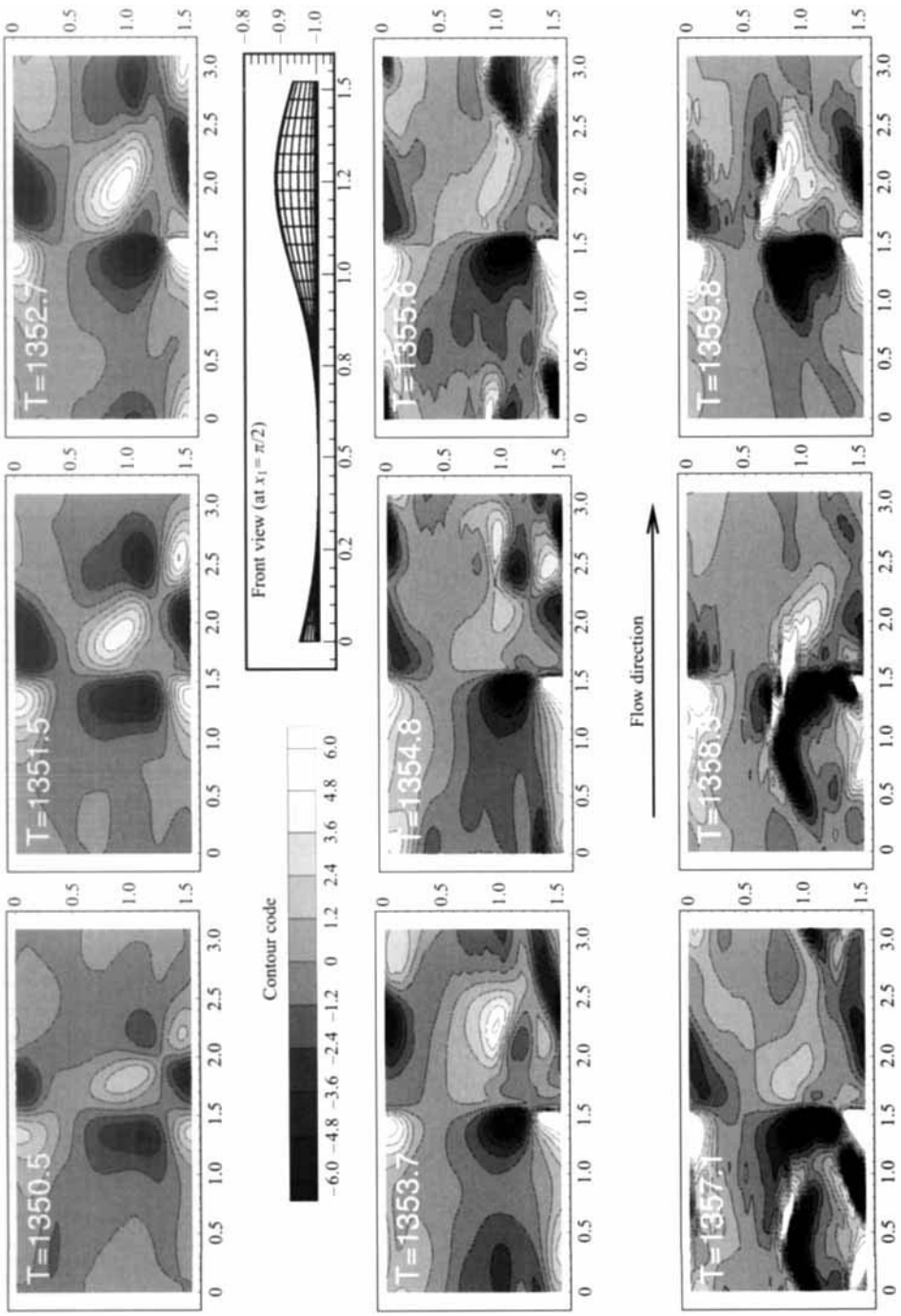

FIGURE 16. A time sequence for Case 3: contour plots of the spanwise component of strain rate at the lower wall (in outer units).

on the upstream side that had signified the lifting of high-speed fluid. These two snapshots coincide with times when drag is rising at its fastest rate (from figure 14). At $T = 1359.8$ the structures that had re-entered are gone, the primary upstream structures are re-defined, and drag makes a momentary move downward.

All of this supports the hypothesis that mechanisms for drag reduction here are lifting of high-speed fluid away from the wall, accompanied by the replacement of high-speed fluid with fluid from the low-speed region. In fact, each of the subsequent snapshots (during the second half of the intermittancy cycle) in which the upstream structures are broad in area and re-entered disturbances are either absent or have not yet reached the actuator coincides with a point in time when drag is decreasing. At all other times the opposite is true. Unlike the laminar case, vortex shedding is an ongoing process. From $T = 1358.5$ to near the end of the intermittancy cycle ($T = 1375.0$), three shedding events occur.

Figure 17 is a time sequences of streamwise vorticity contours. The side view (C) is located along the edge of the high-speed streak ($x_3 = 1.0$). The front view (A) is located upstream of the actuator at $x_3 = 1.374$, the back view (B) downstream at $x_3 = 1.767$. The negative structure in view C at $T = 1350.5$, which extends from the downstream side of the actuator through the outlet and back in at the inlet, is actually pre-existing vorticity associated with the turbulence and is not generated by the actuator.

At $T = 1351.6$ all of the actuator-induced vorticity is present, including a new, positive structure upstream and farthest from the wall (view C) whose source is inertially turned boundary layer vorticity. Motion of the boundary has intensified all of the structures. One time unit after the actuator stops, at $T = 1353.7$, vortex shedding commences. The event occurs sooner than in the laminar case, catalyzed by nearby structures associated with the turbulent field.

At $T = 1355.6$ the shed vortices have re-entered the box and are approaching the actuator. By their proximity overhead at $T = 1357.1$, they begin to disrupt the lifting process (views A and C) and drag is on the rise. At $T = 1358.5$ the upwash pair upstream of the actuator is completely destroyed (view A), drag is increasing rapidly, and another set of vortices has been shed. Again, shedding occurs only once in the laminar case. By $T = 1359.8$ the oldest, most intense structures have come full-circuit and they combine with newer vorticity downstream of the actuator, precipitating another break in the wake region at $T = 1362.5$ (not shown). The process continues with breaks between $T = 1365.1$ and $T = 1366.6$ and at $T = 1371.4$.

Just as the field itself is unsteady, so is the wake – even though the local Reynolds number is well below the value at which the wake in a laminar flow becomes turbulent (referring here to a Reynolds number based upon actuator height and the average, local velocity that would exist through the height interval absent the actuator). Attitudes of the vortical structures – proportional to the ratio of actuator speed to local velocity – are more vertical in the laminar case, so that even though one set of detached vortices does re-enter the box, it is located well above the actuator and does not interact to any great extent with the newest structures.

Analysis of flow over a solitary actuator rising into a turbulent wall layer will require removal of periodic boundary conditions in the streamwise direction. One might guess that vortex shedding subsequent to the first event will be less frequent: without the cumulative effects of re-circulating disturbances, the detached structures would be less intense. Figure 18 is a time sequence of streamwise vorticity in a plane at $x_2^+ = 3$. The view plane cuts through structures close to the wall, those generated by spanwise pressure gradients at the wall.

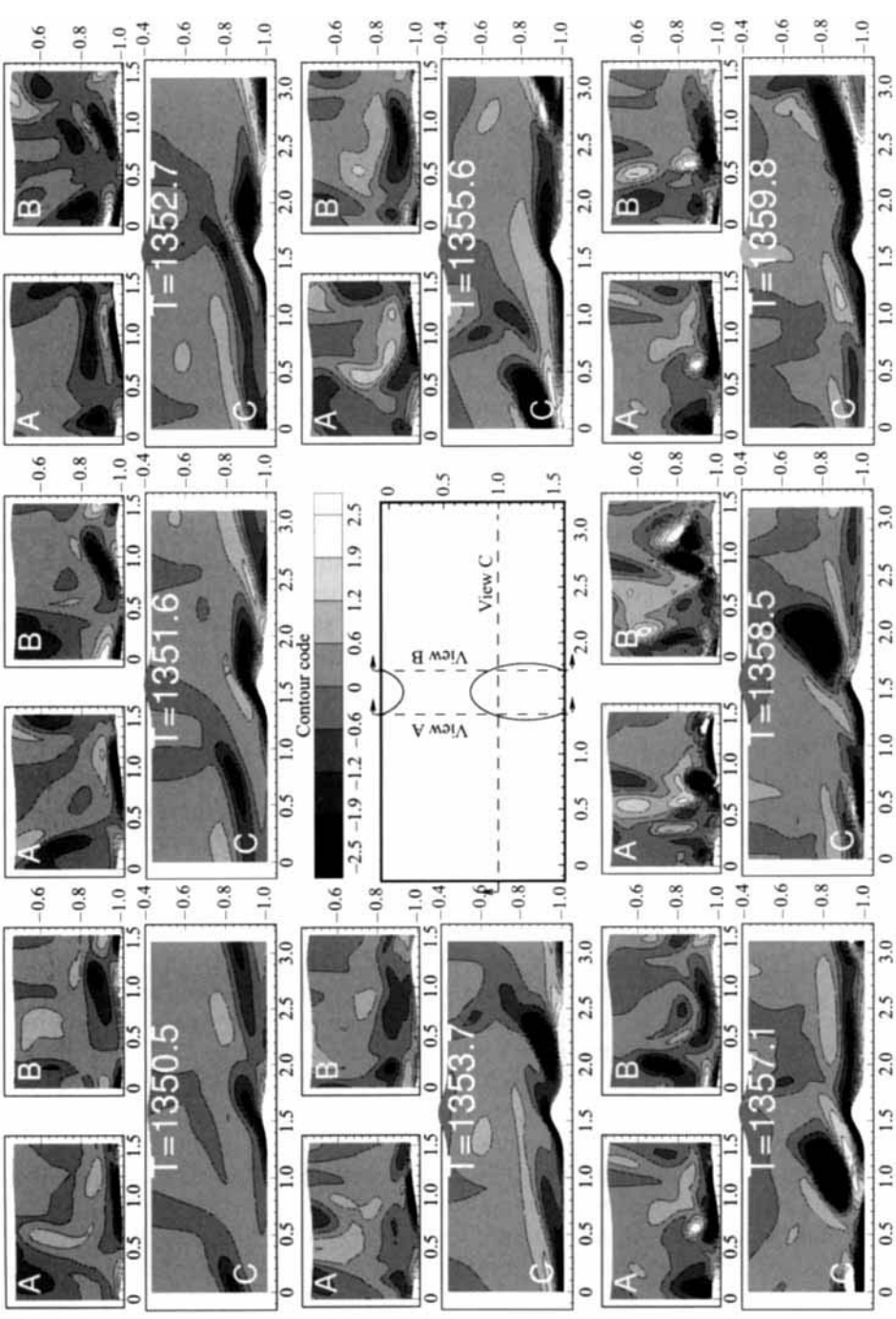

FIGURE 17. A time sequence for Case 3; contour plots of streamwise vorticity (in outer units). The side view (C) is located along the edge of the high-speed streak ($x_3 = 1.0$). The front view (A) is located upstream of the actuator (at $x_1 = 1.374$), the back view (B) downstream (at $x_1 = 1.767$).

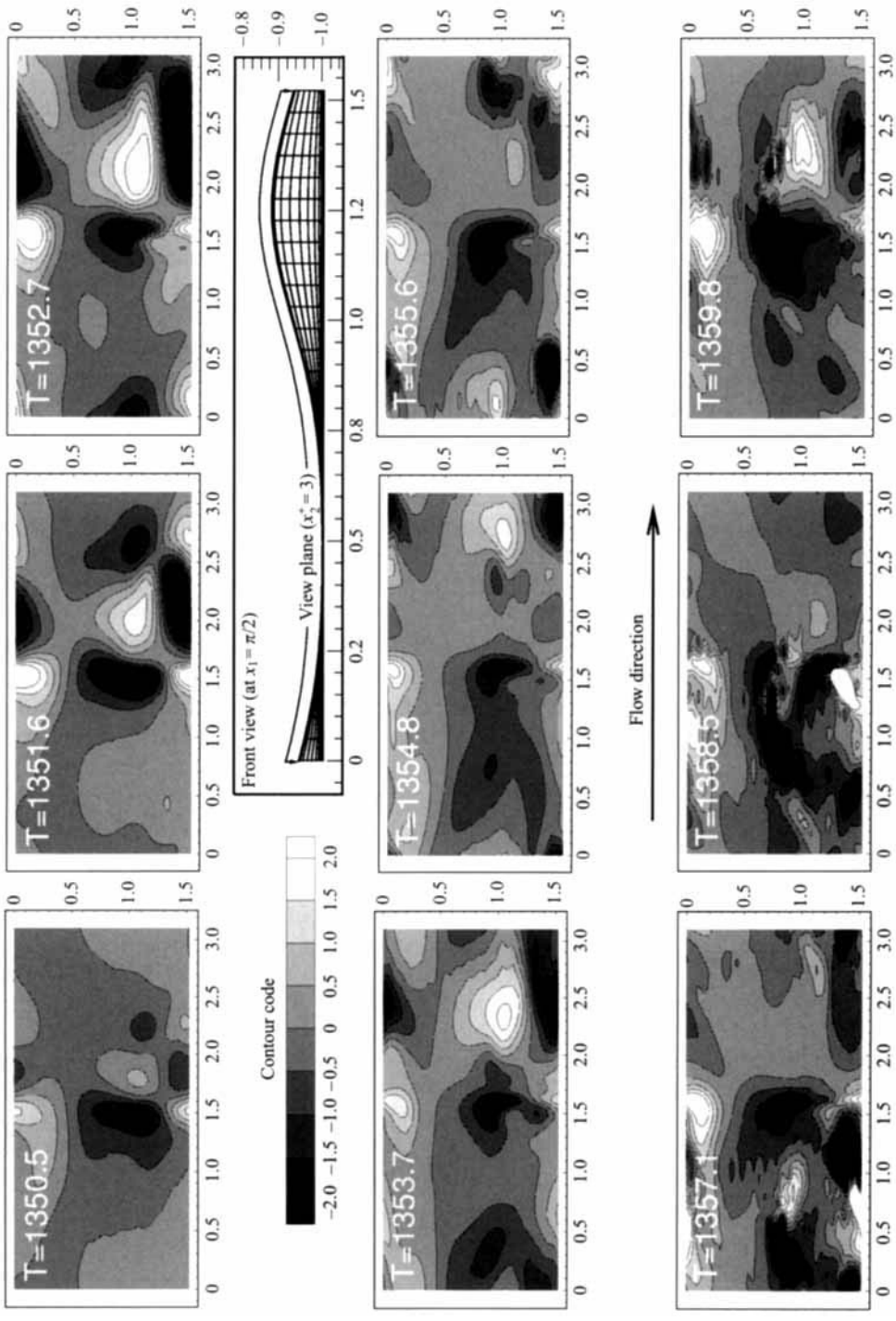

FIGURE 18. A time sequence for Case 3: contour plots of streamwise vorticity (in outer units). The view plane is located at $x_2 = -0.97$ ($x_2^+ = 3$).

Here the vortical structures divert flow around the actuator, producing the upstream upwash and downstream downwash. If the upwash pair decreases drag by lifting high-speed fluid, then it follows that the downwash pair would have a deleterious effect. Because the downstream pair is centred over a region of separated flow, the adverse effect is mitigated. Nonetheless, a strong and widespread downwash may account for some of the smaller increases in drag.

For instance, the region of separation has contracted at $T = 1353.7$, limning a figure-eight (∞) on the wall in figure 15. From figure 18 the downwash vortex pair is strong at $T = 1352.7$ and $T = 1353.7$, covering a broad area behind the actuator. And from figure 14, drag increases through the interval. Both phenomena probably account for the direction that mean drag takes: optimal conditions consist of a broad area of upstream upwash with a minimal amount of downwash downstream. Detached vortices that re-enter the box are clearly responsible for the most dramatic increase in drag, at $T = 1358.5$, by destroying entirely the upstream upwash.

Last is a time sequence of surface stress patterns (figure 19). Again, streamlines are constructed from the stream- and spanwise components of the strain rate, and they indicate flow direction close to the wall. As the actuator rises ($T = 1350.5$ and $T = 1351.6$) a zone of separation appears downstream, and it grows in time. The actuator stops at $T = 1352.7$ and at this point low-speed fluid is clearly funnelling into the wake region. Subsequently, at $T = 1353.7$, flow re-attaches at points downstream and the fluid that was stagnated on the upstream side detaches. This coincides with the first shedding event. At $T = 1358.5$ the symmetric pattern atop the actuator has disintegrated and drag is zooming upward. At $T = 1359.8$ the pattern re-forms and drag momentarily decreases.

The actuators of Cases 1, 2, and 3 were raised at the beginning of the intermittency cycle only as a matter of convenience. Envisioned is an array of sensors that measure strain, linked to an array of actuators. Where the strain exceeds a threshold value, an actuator is raised. Having identified a high-speed streak, an actuator raised will remain up through the life of the streak, which may span many cycles. Short runs in which an actuator is raised under the high-speed streak at different times during the intermittency cycle confirm that drag reduction is effected regardless of the state of the flow.

In two final tests, the actuator positioned under the low-speed streak (Case 2) is lowered. The actuator is retracted at full-speed ($\dot{\varepsilon}_* = u_*$) in Case 4 and at half-speed ($\dot{\varepsilon}_* = \frac{1}{2}u_*$) in Case 5. Constrained by the excessive computational expense, this is a shorthand approximation of the actual scenario in which an actuator that has been raised under a high-speed region is subsequently lowered, as a low-speed region drifts over it.

Figure 20 contains Case 0, 4, and 5 time histories of the mean streamwise strain rate at the wall. The actuators of Cases 4 and 5 begin to drop at $T_S = 1362.1$. The faster moving actuator (Case 4) is fully retracted at $T_F = 1365.0$ and the slower moving actuator (Case 5) at $T_F = 1367.4$. Significant increases in drag occur as the actuators are lowered. A contour plot of wall-normal velocity (on the actuator centreplane) indicates that the vertical velocity of the fluid peaks at a point just above the top of the actuator.

This negative wall-normal component drives streamwise momentum toward the wall and dramatically increases the strain rate on and behind the actuator as it falls. In addition, momentum from the adjacent high-speed region is drawn toward the collapsing actuator. This results in an expansion of the high-speed region and contributes to the increase in drag.

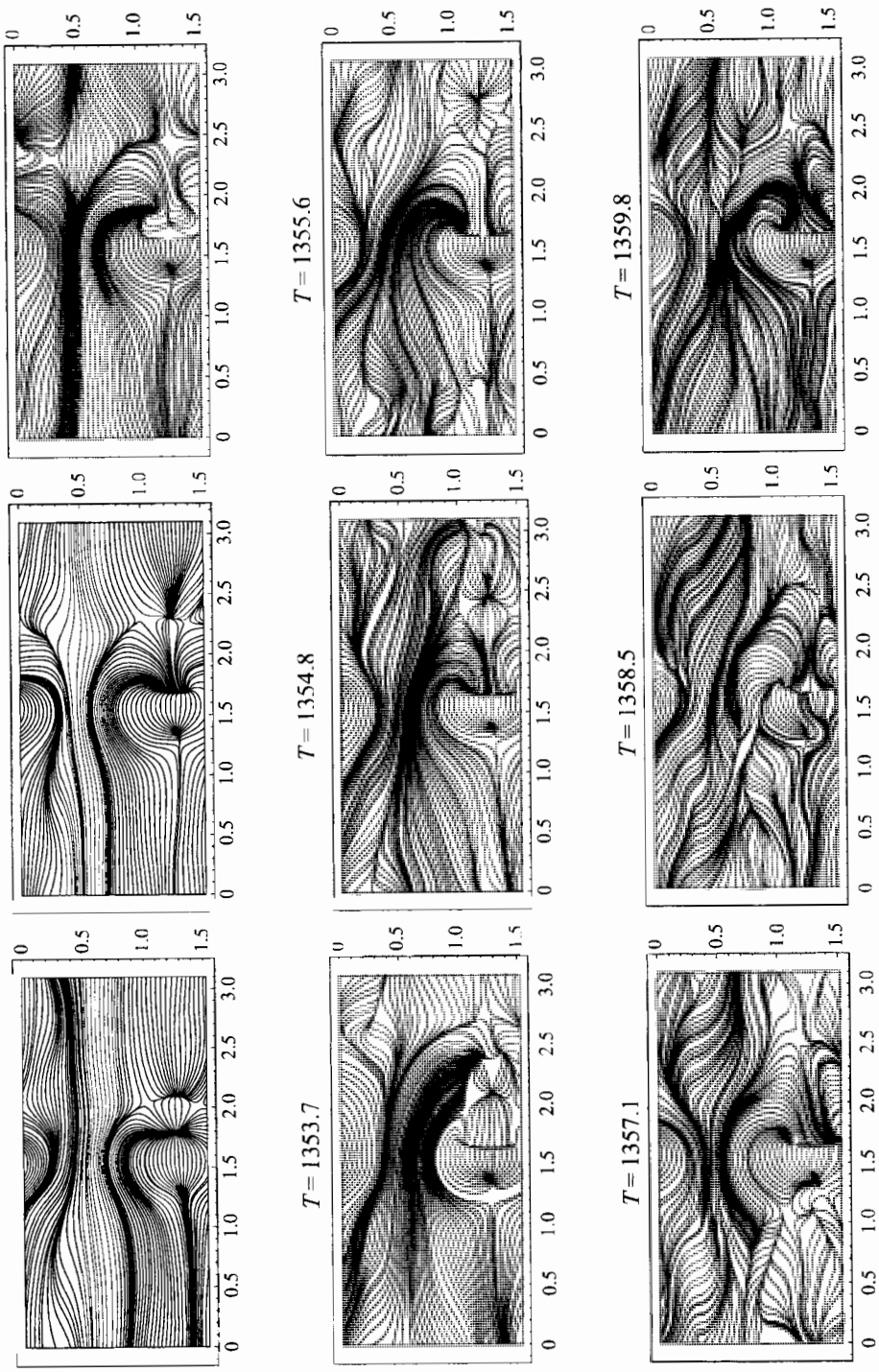

FIGURE 19. A time sequence for Case 3: surface stress patterns. Streamlines are constructed from the stream- and spanwise components of the strain rate and indicate the direction of flow close to the lower wall.

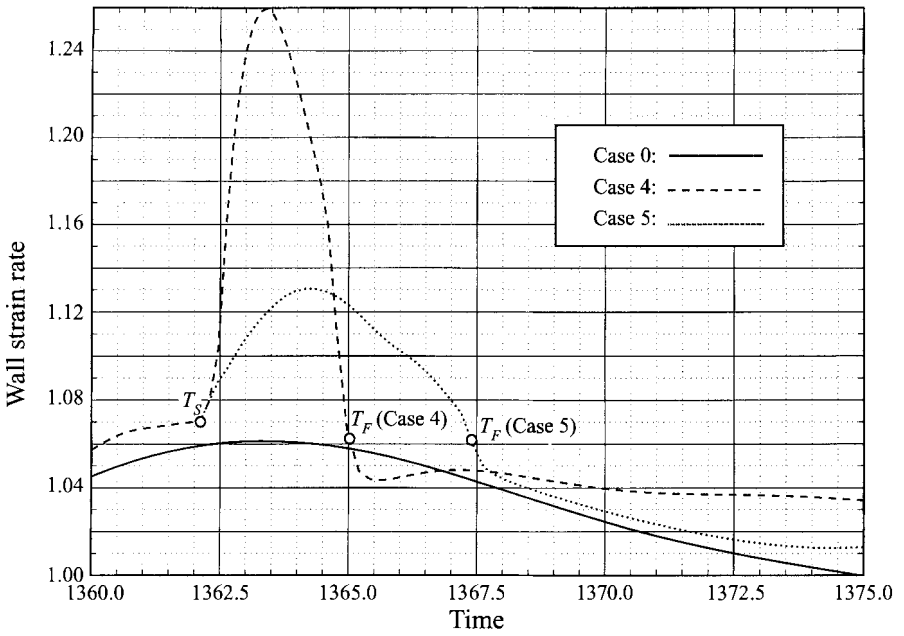

FIGURE 20. Time histories for Cases 0, 4, and 5 of the mean streamwise strain rate at the lower wall, normalized with the Case 0 time-averaged value (Ω_w). The Case 4 and 5 actuators begin to drop at T_S and are fully retracted at T_F.

Case	% Change in drag (ϕ)
1	−2.1
2	+1.4
3	−6.8
4	+3.9
5	+2.4

TABLE 4. Summarized results of the control simulations

Table 4 summarizes the results of the control simulations. The percentage change in skin friction drag (ϕ) is defined as follows:

$$\phi_i = \left[\frac{\int_{T_a}^{T_b} F^i \mathrm{d}t}{\int_{T_a}^{T_b} F^0 \mathrm{d}t} - 1 \right] \times 100\%. \tag{4.3}$$

$F^i(t)$ and $F^0(t)$ are the spatially averaged values of drag at the wall for Cases i and 0, respectively. For Cases 1, 2, and 3, $T_a = 1349$ and $T_b = 1375$. For Cases 4 and 5, $T_a = 1362$ and $T_b = 1375$. As was previously noted, the actuators of Cases 1, 2, 4, and 5 are smaller and symmetric; the Case 3 actuator is twice as wide as the others (in the spanwise direction).

5. Conclusions

Summarizing the results, an actuator has been used to control (or change) the skin friction drag at one of the walls of a minimal flow unit. Although streamwise periodicity produces conditions that hamstring the efficacy of the actuator, matching fluctuations in the mean strain rate with changes in the instantaneous flow field has yielded a fairly precise picture of the mechanisms responsible for drag reduction. With the presence of one pair of coherent structures, the controlling mechanism is as follows: raising an actuator underneath a high-speed streak lifts the faster moving fluid away from the wall and allows fluid from an adjacent low-speed region to expand.

This increases the total amount of low-speed fluid near the wall (and decreases the amount of high-speed fluid), which reduces the mean streamwise strain rate. Conversely, raising an actuator underneath a low-speed streak allows the adjacent high-speed region to expand, thereby increasing skin drag. Were the lifting of momentum away from the wall the only dynamic event, then drag reduction would be effected regardless of actuator placement. The Case 2 simulation demonstrates that the process is two-fold, involving lateral displacement of adjacent fluid in conjunction with the lifting.

As was stated in the Introduction, flow in a minimal unit is only a caricature of fully developed channel flow. Discrepancies in the statistics, as identified in §3, are attributable to the fact that only one pair of coherent structures exists. Given the complex nature of interactions between pairs of structures in a true turbulent field, it is remarkable that the minimal unit statistics match as closely as they do.

When considering the results of the experiments presented here, one must bear in mind the statistical differences that do exist – as well as differences in the lateral drift rate of the streaks and in the degree of communication between the flows at each wall. With these caveats and within the context of short-term control, critical features of the flow are adjacent regions of high- and low-speed fluid. This signature is shared by fully developed channel flow and the minimal unit flow. Given this type of flow pattern, the actuator may be used to redistribute momentum close to the wall and thereby control wall shear stress.

Simulations in the minimal flow unit leave open some important questions. Will the dynamics of momentum redistribution be the same in the presence of a multiplicity of coherent structures (and actuators)? Moreover, does the narrow width of the domain have an artificial effect upon the process – on the interplay between and transmutation of the high- and low-speed regions? These questions may be answered either through simulations in a larger domain or through experiments in the laboratory.

Open to question, too, is how one should interpret the impact that streamwise periodicity has upon the control results. Averaged over the time interval of figure 14, the drag reduction achieved in Case 3 is approximately 7%. From the discussion in §4, it seems reasonable to assume that the percentage will be different in the case of a solitary actuator. Without the sharp rise in drag beginning at $T = 1356$ in figure 14 – attributable to recirculated vortices – the drag reduction would be greater. The question becomes whether under real conditions, say on a wing, vortices shed from an actuator upstream will cripple the effectiveness of the next device down.

The vortices do survive far downstream, approximately three box lengths or 900 wall units. They also lose strength as they go. Assuming one actuator per streak with an average streak length of 900 wall units, one may speculate that interference between actuators will be less than that which occurs in the Case 3 simulation. The

fact that some of the high-speed streaks will not be positioned in tandem but will be staggered in the spanwise direction would support this guess. However, the question may only be answered, computationally at least, by removing the periodic boundary conditions in the streamwise direction.

The significant increase in drag that accompanies retraction of an actuator poses a serious problem for the overall control strategy. Based upon the results of Cases 1 and 5 (see table 4), the net change in drag effected by an actuator during a cycle (consisting of raising it once and then lowering it) is slightly positive – at least with the actuator speeds that have been used. From a comparison of Cases 4 and 5, the drag increase that accompanies retraction is proportional to retraction speed.

However, the longer retraction time associated with a slower moving actuator offsets, to a degree, the benefits gained from a reduction in speed. Presumably, some optimal retraction speed exists that minimizes the average increase in drag. The idea would be to slowly lower the actuator as a low-speed region *slowly* drifts over it. Still, it is not clear that such a scheme would produce substantially better net reductions in drag.

Numerical stability constraints have placed limitations upon the range of heights and shapes that may be assigned to an actuator. The strength of upwash vorticity is proportional to both height and aspect, so that a taller actuator with a steeper frontside will presumably effect greater reductions in drag – though the cost may increase as well. As in Cases 1 and 2, form drag associated with the Case 3 actuator is minimal, less than 0.5% of the time-averaged skin drag.

Although the numerical method produces conditions that are less than ideal in an exploration of active control in a turbulent wall layer, it has provided new information on the subject: the identification of a basic mechanism for controlling the skin friction drag. Because of the detail in information they provide and the ease with which parameters may be changed, simulations such as those presented here will be important in complementing experimental efforts directed at smart skin control. Modifications to the algorithm would be a logical next step in the investigation – removal of streamwise periodicity, adjustments to accomodate a wider range of actuator prototypes, and improved computational efficiency (to permit simulations in a box large enough to house several complete sets of coherent structures).

The research was supported by Contract No. F49620-92-J-0287 jointly funded by the US Air Force Office of Scientific Research (Control and Aerospace Programs) and the US Office of Naval Research. Computational resources were provided by the National Science Foundation Supercomputer Facility located at Cornell University. The authors thank H. Fossel and his graduate students at the University of Arizona for graciously allowing H. C. access to their computer facilities.

REFERENCES

BACHER, E. V. & SMITH, C. R. 1985 A combined visualization-anemometry study of the turbulent drag reducing mechanisms in triangular micro-groove surface modifications. *AIAA Paper* 85-0548.

BLACKWELDER, R. F. & ECKELMANN, H. 1979 Streamwise vortices associated with the bursting phenomenon. *J. Fluid Mech.* **94**, 577–594.

BRUSE, M., BECHERT, D. W., HOEVEN, J. G. TH. VAN DER, HAGE, W. & HOPPE, G. 1993 Experiments with conventional and with novel adjustable drag-reducing surfaces. In *Near-Wall Turbulent Flows* (ed. R. M. C. So, C. G. Speziale & B. E. Launder), pp. 719–738. Elsevier.

CANUTO, C., HUSSAINI, M. Y., QUARTERONI, A. & ZANG, T. A. 1988 *Spectral Methods in Fluid Dynamics*. Springer.

CARLSON, H. A., BERKOOZ, G. & LUMLEY, J. L. 1995 Direct numerical simulation of flow in a channel with complex, time-dependent wall geometries: a pseudospectral method. *J. Comput. Phys.* **121**, 155–175.

CARLSON, H. A. & LUMLEY, J. L. 1996 Flow over an obstacle emerging from the wall of a channel. *AIAA J.* **34**, 924–931.

CHOI, H., MOIN, P. & KIM, J. 1994 Active turbulence control for drag reduction in wall-bounded flows. *J. Fluid Mech.* **262**, 75–110.

CHU, D. C. & KARNIADAKIS, G. E. 1993 A direct numerical simulation of laminar and turbulent flow over riblet-mounted surfaces. *J. Fluid Mech.* **250**, 1–42.

COLLER, B. D., HOLMES, P. & LUMLEY, J. L. 1994 Interaction of adjacent bursts in the wall region. *Phy. Fluids* **6**, 954–961.

CORINO, E. R. & BRODKEY, R.S. 1969 A visual investigation of the wall region in turbulent flow. *J. Fluid Mech.* **37**, 1–30.

GAL-CHEN, T. & SOMERVILLE, R. C. J. 1975 On the use of co-ordinate transformation for the solution of the Navier–Stokes equations. *J. Comput. Phys.* **17**, 209–228.

GOTTLIEB, D., HUSSAINI, M. Y. & ORSZAG, S. A. 1984 Theory and applications of spectral methods. In *Spectral Methods for Partial Differential Equations* (ed. R. G. Voigt, D. Gottlieb & M. Y. Hussaini), pp. 1–54. Society for Industrial and Applied Mathematics.

JIMENEZ, J. & MOIN, P. 1991 The minimal flow unit in near-wall turbulence. *J. Fluid Mech.* **225**, 213–240.

KIM, J., MOIN, P. & MOSER, R. 1987 Turbulent statistics in fully developed channel flow at low Reynolds number. *J. Fluid Mech.* **177**, 133–166.

KLEISER, L. & SCHUMANN, U. 1980 Treatment of incompressibility and boundary conditions in 3-D numerical spectral simulations of plane channel flows. In *Proc. 3rd GAMM Conf. Numerical Methods in Fluid Mechanics* (ed. E. H. Hirschel), pp. 165–173. Vieweg, Braunschweig.

KLINE, S. J., REYNOLDS, W. C., SCHRAUB, F. A. & RUNDSTADLER, P. W. 1967 The structure of the turbulent boundary layer. *J. Fluid Mech.* **30**, 741–773.

LAURIEN, E. & KLEISER, L. 1989 Numerical simulation of boundary-layer transition and transition control. *J. Fluid Mech.* **199**, 403–440.

LUMLEY, J. L. 1973 Drag reduction in turbulent flow by polymer additives. *J. Polymer Sci.* D: *Macromol. Rev.* 7, 263–290.

MASON, P. J. & MORTON, B. R. 1987 Trailing vortices in the wakes of surface-mounted obstacles. *J. Fluid Mech.* **175**, 247–293.

NAKAGAWA, H. & NEZU, I. 1981 Structure of space-time correlations of bursting phenomena in an open-channel flow. *J. Fluid Mech.* **104**, 1–43.

ROBINSON, S. K. 1991 The kinematics of turbulent boundary layer structure. *NASA Tech. Mem.* 103859, pp. 401–404.

SMITH, C. R. & METZLER, S. P. 1983 The characteristics of low-speed streaks in the near-wall region of a turbulent boundary layer. *J. Fluid Mech.* **129**, 27–54.

SPALART, P. R., MOSER, R. D. & ROGERS, M. M. 1991 Spectral methods for the Navier–Stokes equations with one infinite and two periodic directions. *J. Comput. Phys.* **96**, 297–324.

VIRK, P. S. 1975 Drag reduction fundamentals. *AIChE J.* **21**, 625–656.

VOKE, P. R & COLLINS, M. W. 1984 Forms of the generalised Navier–Stokes equations. *J. Engng. Maths* **18**, 219–233.

WALSH, M. J. 1980 Drag characteristics of v-groove and transverse curvature riblets. In *Viscous Flow Drag Reduction* (ed. G. R. Hough), pp. 168–184. AIAA.